2019

Quantifying Air-Sea Gas Exchange at High Wind Speeds Using Noble Gas Measurements: Insights from the SUSTAIN Wind-Wave Tank

Lumi Kinjo
lkinjo@wellesley.edu

Quantifying Air-Sea Gas Exchange at High Wind Speeds Using Noble Gas Measurements: Insights from the SUSTAIN Wind-Wave Tank

Lumi Kinjo
Advisor: Rachel H.R. Stanley, Ph.D.
Department of Chemistry, Wellesley College

Submitted in Partial Fulfillment of the
Prerequisites for Honors in Chemistry
April 2019

Acknowledgements

I would like to first thank my advisor, Professor Rachel Stanley who has taught me how to think and communicate as a scientist. You have also shown me what it means to hold oneself to the highest standard, while also being a giving and compassionate person. Whenever I visited your office, I left the room feeling more cheerful (and often with a cup of tea in hand) because of your radiant positivity. Thank you for all of your mentorship and encouragement you have given me throughout my time at Wellesley. You are my inspiration, and I will miss you so much when I leave the college.

Thank you so much to my thesis committee members, Professors Nolan Flynn, Mala Radhakrishnan, and Corinne Gartner. Together, you have provided me with such a supportive environment to pursue this thesis project. Nolan—I really appreciated your extensive knowledge in instrumentation and analytical techniques. Analytical Chemistry was also one of my favorite classes and I am grateful for your continued mentorship and advice you have given me. Mala—thank you so much for generously agreeing to be on my thesis committee though I was never a student in your classes. Your questions and comments have provided me with new insights and challenged me to think outside of the box. Corinne—I am grateful that you kindly agreed to be my honors visitor. You taught me about ways to think about difficult questions critically. I would also like to thank Sarah Barbrow, for her patience and guidance in helping me with citations.

I would like to take a moment to thank my family members, who have always given me support and encouragement. We have often been scattered around the world, but the physical distance never mattered too much because you are close and dear to my heart. A special thank you to my Wellesley host mother, Louise Treitman ’74 for taking great care of me since the day I arrived at the airport as a first year. I would also like to thank Aris for his encouragement and advice.

Finally, I would like to thank Stanley lab members, Helene Alt ’DS, Emily Kopp ’20, and Danielle Aldrett ’21 whom I traveled and conducted experiments in Miami together. We were truly a dream-team and I feel so lucky to have met you. I would also like to thank Callan Krevanko ’18 for her thesis work from previous year in founding the grounds of my thesis. Another big thank you to Andrew Wyatt Smith at the University of Miami for providing us with the bubble data and always answering my questions so kindly. I would also like to thank the National Science Foundation (Grant OCE-1634467), Jerome A. Schiff Fellowship, and Wellesley Science Center Summer Research Program for their generous support.

Table of Contents

Abstract

Gas exchange at high wind speed is not well understood—few studies have been conducted at wind speeds above 15 m s^{-1}, and significant disagreement exists between gas exchange models at high wind speeds. In particular, the flux due to bubbles is not explicitly included in many gas exchange models, despite the fact that bubble-mediated gas exchange becomes increasingly important at higher wind speeds. The goal of my thesis project is to quantify air-sea gas exchange under high wind speeds and to examine the relationship between noble gas measurements, bubble spectra, wave-type, and water temperature. Noble gases serve as excellent tracers for this purpose, as they are biologically and chemically inert, and have a wide range of solubility and diffusivity that responds differently to physical forcing.

Over the course of five days, we conducted 35 experiments at the SUrge STructure Atmospheric InteractioN (SUSTAIN) wind-wave tank with wind speeds at 20 - 50 m s^{-1}, water temperatures at 20°C, 26°C, and 32°C, and wave conditions including uniform (regularly breaking) waves and JONSWAP (random, real ocean-like) waves. Continuous Ne, Ar, Kr, and Xe ratio measurements were obtained by a Gas Equilibration Mass Spectrometer (GEMS). Additionally, discrete noble gas measurements were collected at the beginning of select experiments and at the end of all experiments for He, Ne, Ar, Kr, and Xe. Bubble size and volume spectra were obtained using an underwater shadowgraph imaging device. Other physical measurements such as continuous salinity, water temperature, wind/wave velocities, and atmospheric pressure were also obtained.

Our result from the conditions with the highest saturation anomalies suggests that steady state saturation anomalies of gases level off as wind speed increases. Additionally, both the temperature dependence of noble gas saturation anomalies and the coherence between bubble surface area spectra and saturation anomalies suggest that partially dissolving bubbles may have an important flux contribution at higher wind speeds. Since the SUSTAIN wind-wave tank is much shallower than the real ocean, we cannot directly apply our results to the ocean to make predictions. Nonetheless, the relationship between gas flux and bubble size spectra, wind, and wave conditions learned from this work provide us with

important insights to improve gas exchange models.

Chapter 1. Introduction

1.1. Background

The ocean serves as the largest sink for anthropogenic CO_2 in the atmosphere, taking up about one-third of the CO_2 released in the air by humankind (Sabine et al., 2004). Since the industrial revolution in the late 18th century, large quantities of CO_2 have been emitted from burning fossil fuels. Study of air-bubbles trapped in the Antarctic ice cores shows that the present-day level of CO_2 is unprecedented over the past 420,000 years (Petit et al., 1999). The atmospheric CO_2 level has increased from ~280 ppm in the pre-industrial level (Petit et al., 1999) to over ~400 ppm in recent years (Keeling et al., 2019). Without the oceanic uptake, it is estimated that the atmospheric CO_2 would be significantly higher today than the current observation (Sabine et al., 2004). Consequently, better parametrization of the oceanic uptake process of climatically relevant gases is important in developing models to calculate global gas flux and to make accurate climate predictions (Carpenter et al., 2012; Pozzer et al., 2006).

Exchange of gases between the air-sea interface is often quantitatively expressed in terms of flux, F (mol $m^{-2}s^{-1}$), which is the product between gas transfer velocity k (cm h^{-1}) and difference in concentration of the gases dissolved in water, C_w, and the equilibrium value of the gas, C_{eq} as shown in Equation 1 (Asher et al., 1996; McNeil and D'Asaro, 2007; Pozzer et al., 2006; Wanninkhof et al., 2009):

$$F = k (C_w - C_{eq}). \quad \text{(eq 1)}$$

By convention, F is negative for gas flux from the atmosphere to the ocean. C_{eq} can be calculated from Henry's law,

$$C_{eq} = H_{cp} \times P_{air}, \quad \text{(eq 2)}$$

where H_{cp} (mol $m^{-3}atm^{-1}$) is the Henry's law constant, which depends on water temperature and salinity, and P_{air} (atm) is the partial pressure of the gas in the atmosphere. Gas transfer velocity k is a function of factors such as turbulence, boundary layer depth, kinematic viscosity of water, and molecular diffusivity of the gas (Wanninkhof et al., 2009).

Because gas transfer velocity was shown to be related to the turbulence at the air-

water interface, k is often parameterized as a function of wind speed 10 m above the ocean surface, U_{10} (m s^{-1}). Over the past few decades, laboratory and field studies have led to many representative models that describe the relationship between gas transfer velocity and wind speed, including segmented linear (Liss and Merlivat, 1986), quadratic (Ho et al., 2006; Wanninkhof, 1992), cubic (Wanninkhof and McGillis, 1999), and somewhere in between segmented linear and quadratic (Nightingale et al., 2000). The quadratic relationship was developed by incorporating the data from averaged gas transfer velocity and wind speed derived from oceanic bomb-^{14}C uptake and is the most widely used parameterization (Wanninkhof, 1992). A compilation of proposed relationships between gas transfer velocities are presented here, including the four studies discussed above (Figure 1).

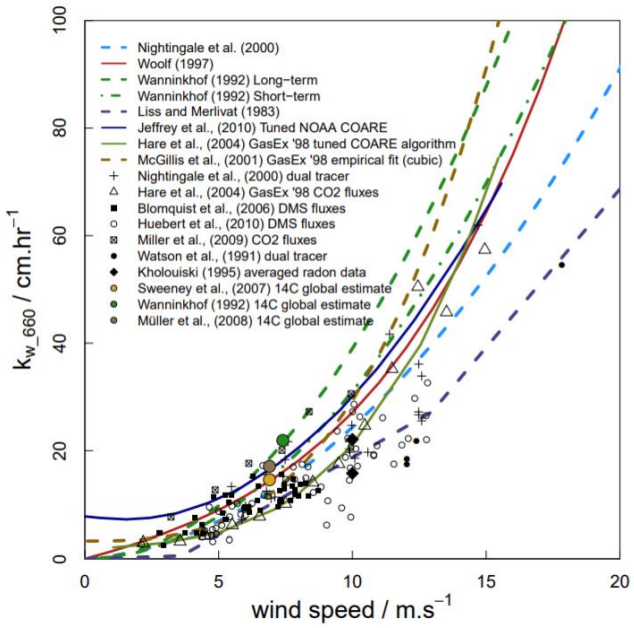

Figure 1. Comparison of proposed relationships between gas transfer velocity and wind speeds. Few measurements are taken above 15 m s^{-1} and significant disagreement exists between predicted relationships at higher wind speeds. Figure reproduced from Johnson, 2010.

As shown in the figure above, the proposed relationships between gas transfer velocity and wind speed show significant disagreement at higher wind speeds (Johnson, 2010). One of the reasons behind this observation is due to bubble entrainment, a factor not explicitly included in most wind speed-only parameterization. As it has been shown that flux

due to bubbles significantly enhance gas exchange at high wind speeds (McNeil and D'Asaro, 2007), a more accurate expression of the total gas flux would be as below:

$$F_{total} = k\,(C_w - C_{eq}) + F_{bubbles}. \quad \text{(eq 3)}$$

In fact, many of the field studies investigating air-sea gas exchange explicitly incorporate the contribution of bubbles in determining the gas flux (Liang et al., 2013; McNeil and D'Asaro, 2007; Stanley et al., 2009b). Few studies, however, have been conducted to measure gas exchange at high wind speeds where the bubble mediated gas exchange becomes increasingly important.

Bubbles enhance gas transfer between the water and the atmosphere by providing additional pathway for gas exchange other than the ocean surface. When the hydrostatic pressure overcomes the surface tension, bubbles can also inject gases into the surrounding seawater, even when the water is supersaturated (Liang et al., 2013). Since bubbles are generated by breaking waves, their effect on air-sea gas exchange is especially prominent in turbulent conditions. Bubble creation occurs in two phases—in the first phase, bubbles are actively created from the moment of wave breaking, as the air inside the breaking wave crest is entrained and fragmented. Once the active bubble creation process ceases, the second phase begins, in which the newly created bubble plume undergoes constant changes due to turbulence, buoyancy, and gas exchange (Deane and Stokes, 2002). Bubble mediated gas exchange is a highly complex process, influenced by a variety of correlational factors, such as degree of bubble dissolution, bubble distribution, temperature, and presence of surfactants. Little is known about the effect of different parameters that determine bubble mediated gas exchange.

1.2. Methods to study air-sea gas exchange

Measurement of gas transfer velocity and fluxes can be broadly separated into three categories: direct flux measurement, bulk concentration, and proxy methods (Wanninkhof et al., 2009). Here is a brief description of each method and examples of its application:

1. Direct flux measurement approach

Flux in the air above the ocean surface and ΔC_w can be directly measured to

determine gas transfer velocity, k, using Equation 1. An example of the direct measurement approach is eddy correlation, or, covariance technique. The covariance technique is considered to be one of the best ways to determine F as it does not depend on assumptions on gas properties or turbulent structure at the atmospheric boundary layer (Wanninkhof et al., 2009). The main challenges of this measurement method are reducing the effect of platform motion when estimating the flux, minimizing the effect of flow distortion from the vessel movement, and low signal-to-noise ratio. The covariance technique has been successfully used to measure gases such as CO_2 in the open ocean (McGillis et al., 2001).

2. Bulk concentration approach

In the bulk concentration approach, measurement of C_a (concentration of gas in air) and ΔC_w over time is used to calculate F and k. Given the water volume and surface area are known, flux can be calculated by multiplying ΔC_w and volume-to-surface ratio. Once the flux is known, k can be derived using Equation 1 and C_a and C_w values. An example of the bulk concentration approach is the $^3He/SF_6$ double tracer method, in which the concentration of gases in water and air are out of equilibrium (Wanninkhof et al., 2009). In this method, known ratio of ^3He and SF_6 are released into the ocean and gas transfer velocity is determined from the change in $^3He/SF_6$ ratio (Ho et al., 2006; Nightingale et al., 2000). By injecting gases that are not naturally abundant, it can minimize the impact of biological processes on measurements of gas exchange (Wanninkhof et al., 2009).

3. Proxy technique

Nongaseous tracers can be used as proxies to measure air-sea flux more easily. Field applications, however, are typically limited to thermographic techniques using infrared (IR) imagers which assumes that the transfer velocity of heat can be directly related to that of gases. The advantage of this method is that it does not require the correction for ship motion, unlike the eddy correlation, since the turbulence signal is much larger than the platform motion (Wanninkhof et al., 2009).

Our approach of measuring air-sea gas exchange can be broadly categorized into the bulk concentration approach. This is because we measure gas abundance in the water and the

air but do not directly measure the flux. In our study, we obtained continuous measurements of Ne, Ar, Kr, and Xe mole ratios in real-time using a recently developed field deployable Gas Equilibration Mass Spectrometer (GEMS) (Manning et al., 2016). GEMS cannot measure He since it is permeable to the system. Additionally, we also collected discrete noble gas measurements at the beginning and end of our experiments. The purpose of this was to obtain accurate concentration measurements and to use the measurements to calibrate the GEMS continuous data. GEMS has an accuracy 0.9% or better for all gas ratios when calibrated with air, and the accuracy typically improves to 0.6% or better when calibrated with discrete samples analyzed by traditional in-lab mass spectrometer. The entire system can be easily transported and costs significantly less than the in-lab mass spectrometers (~$50,000). The e-folding time, or τ, where roughly 63% of the gas becomes equilibrated, ranges from 90 - 410 seconds depending on the gas, where Xe is the fastest and Ne is the slowest to equilibrate (Manning et al., 2016). The detailed mechanism of GEMS as well as the sampling and analysis of discrete noble gases are explained in the Methods section (Chapter 2).

1.3. Using noble gases to study air-sea gas exchange

Noble gases are excellent tracers for the physical process of air-sea gas exchange as they are chemically and biologically inert (Stanley and Jenkins, 2013). There are five stable noble gases (He, Ne, Ar, Kr, and Xe), excluding radioactive Rn, and they have a wide range of diffusivity and solubility in sea water (Figure 2).

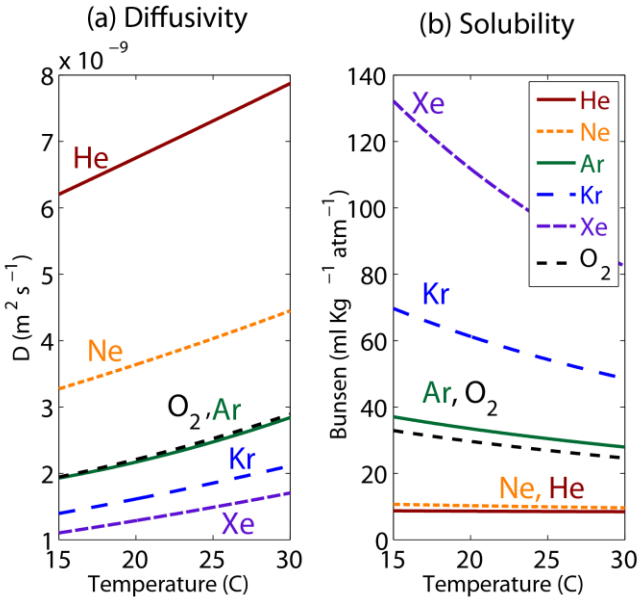

Figure 2. (a) Diffusivity and (b) solubility of five noble gases (He, Ne, Ar, Kr, Xe), O_2 and N_2 as a function of temperature. Figure reproduced from Stanley and Jenkins, 2013.

Lighter gases, such as He and Ne, are less soluble and their solubilities have very little temperature dependence. Heavier gases such as Ar, Kr, and Xe are more soluble and their solubilities change dynamically as temperature changes, which make them useful tracers for thermal forcing. Larger gas molecules have higher solubility than smaller molecules because they have more electrons away from the nucleus. Consequently, larger gas molecules are more easily polarized. Ar is often measured in conjunction with O_2 since its solubility and diffusivity closely align with that of O_2. Concurrent measurements of Ar and O_2 allow the separation of the biological and physical processes of O_2 gas exchange, which is useful in quantifying biological productivity such as net community production (Cassar et al., 2009; Craig and Hayward, 1987; Hamme et al., 2012; Stanley et al., 2010).

The wide range in diffusivity and solubility allows concurrent measurements of multiple noble gases to be especially useful in studying the physical processes of air-sea gas exchange. Specifically, the extent of departure from equilibrium, called saturation anomaly, contains important information about the character and the magnitude of the physical forcing. For example, since there are relatively small amounts of He and Ne dissolved in water, they are especially responsive to bubble injection process (Jenkins, 1988). While noble gases in

the ocean are typically close to equilibrium with the atmosphere, various physical processes such as bubble injection, rapid warming and cooling, and change in salinity pushes them away from equilibrium (Figure 3) (Stanley and Jenkins, 2013). Figure 4 illustrates how the bubble injection process affects the saturation anomaly of gases such as Ne and Xe differently (Hamme and Severinghaus, 2007). Saturation anomaly is defined as the percentage difference between the gas concentrations measured in water and the equilibrium concentration predicted by Henry's Law (eq 2). For instance, saturation anomaly for Ne is:

$$\Delta\mathrm{Ne} = \left(\frac{[\mathrm{Ne}]\mathrm{water}}{[\mathrm{Ne}]\mathrm{equil}} - 1\right) * 100 \qquad \text{(eq 4)}$$

Note: Positive Δgas value means that the gas is supersaturated.

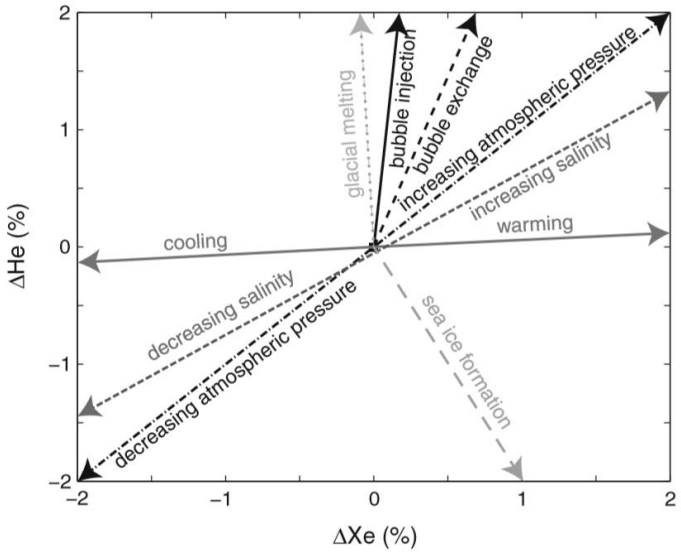

Figure 3. Diagram representing the effect of different physical forcing on saturation anomalies of He and Xe. Due to the differences in solubility and diffusivities of noble gases, measurements of multiple noble gases allow the separation and quantification of different physical processes. Figure reproduced from Stanley and Jenkins, 2013.

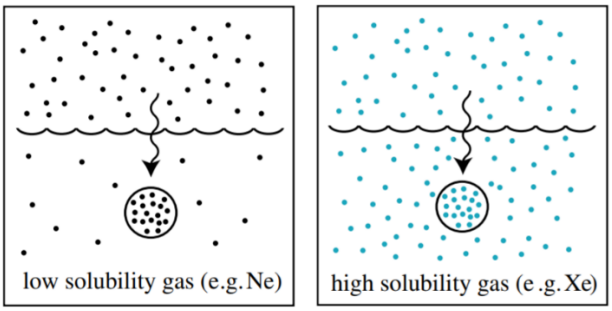

Figure 4. Less soluble gases are affected more by bubble-mediated gas exchange. Since fewer gas molecules are already present in the water, gas injection by bubbles will result in higher saturation anomaly for low solubility gases, such as Ne. Figure reproduced form Hamme and Severinghaus, 2007.

1.4. Studies on bubble mediated gas exchange

This section provides some of the studies exploring different parameterization of bubble mediated gas exchange.

1. Completely vs partially dissolving bubbles

Noble gases, being chemically and biologically inert, have been used to estimate the amount of gas exchange from complete and partial bubble dissolution. In the case in which the bubbles completely dissolve, all the air inside the bubble is "injected" to the surrounding water with the same fractional abundance of gases as the atmosphere. In the case in which the bubbles partially dissolve, the compositions (i.e. gas fraction) of the bubbles change overtime according to the solubility and diffusivity of individual gases. Understanding the relative flux contributions from partial and complete bubble dissolution is important to know the effect of bubble-mediated gas exchange on gases with different solubilities and diffusivities. Additionally, it is useful to understand the effect of bubbles on invasion and evasion. For gas invasion, both partial and complete bubble dissolution matter but for evasion, only partial bubble dissolution matters.

Hamme and Emerson (2006) calculated the flux from completely and partially dissolved bubbles for O_2 using one-year time series measurements of Ne and N_2/Ar near Hawaii, using a forward approach. They found that relative contributions of flux due to completely and partially dissolved bubble were roughly the same for O_2 (Hamme and

Emerson, 2006). Stanley et al. (2009) used measurements of five noble gases (He, Ne, Ar, Kr, and Xe) collected over the period of three years at the Bermuda Atlantic Time series Study (BATS) to constrain bubble mediated gas exchange model. Using the inverse approach, they found that over 95% of the bubble flux stems from completely dissolving bubbles, a much higher estimate than that presented by Hamme and Emerson (2006). Moreover, they found that the flux due to bubbles was substantial in the winter—approximately equal to the diffusive flux—even for soluble gases such as Xe. This highlighted the importance of considering air injection flux for gases such as N_2 and O_2 with solubility similar to or less than Xe (Stanley et al., 2009b).

2. Bubble size distribution

Bubble mediated gas exchange has also been parameterized by bubble size distribution. Bubble size distribution is dependent on the physical mechanism of bubble creation as well as external factors such as temperature. For instance, Deane and Stokes (2002) found that small and large bubbles have different bubble density dependence on the radius and are created in different ways. Bubbles with radius larger than ~1 mm are formed as the air cavity created in between the wave jet and wave face fragments, with bubble density proportional to the bubble radius raised to the power of -10/3. In contrast, smaller bubbles are formed from the interaction between the plunging jet and the drop impact at the wave face, with power-law scaling of -3/2 (Deane and Stokes, 2002).

While Deanne and Stokes (2002) focused on the physical mechanism of bubble creation in the laboratory, Vagle et al. (2012) explored the relationship between temperature stratification and bubble size distribution in the open ocean. Simultaneous measurements of total heat flux, temperature stratification, upper ocean turbulence, and bubble size distribution were taken during a week-long Radiance in a Dynamic Ocean (RaDyO) study conducted near Hawaii. Backscatter data from sonars were used to estimate the extent of bubble size distribution and plume depth. The study suggested that positive heat flux, and the consequent near-surface temperature stratification, decreases turbulence and thus affects bubble field distribution. During periods of day-time high heat flux, there was more temperature stratification and lower turbulence dissipation rates; the number of larger

bubbles with radii greater than 200 μm was also significantly lower compared to that during negative heat flux. Possible reason for this observation was attributed to suppressed near-surface turbulence reducing downward movement of bubbles, leading to fewer larger bubbles at depth as they have faster buoyant rise speed. Strong positive heat flux may have also reduced the intensity of breaking instances and thus resulted in fewer large bubbles (Vagle et al., 2012).

3. Surfactants

Lastly, presence of surfactants, derived from phytoplankton and terrestrial runoffs, for example, also complicates bubble mediated gas transfer in the natural environment. Surfactants decrease the mobility of the bubble interface and influence the bubble gas transfer rate and rise velocity (Leifer and Patro, 2002). "Clean" bubbles that are not contaminated by surfactants have higher gas transfer rate, but since they also have a higher rise velocity, they have a decreased bubble lifetime. Parameterization using surfactants are often simplified using the assumption that while the ocean water is never truly "clean," very large bubbles generally have fluid surfaces and behave as if they are clean bubbles (Goddijn-Murphy et al., 2016; Woolf et al., 2007).

1.5. Using wind-wave tanks to study gas exchange

Wind-wave tanks have been successfully used to study air-sea gas exchange, allowing researchers to conduct experiments under controlled conditions with variable surface states, wind speeds, wave types, and surfactant concentrations. At the Aeolotron tank in Heidelberg, Germany, gas transfer velocity of various gases was determined for wind speeds ranging from 0.73 to 13.2 m s^{-1} and results were found to have a strong reproducibility and comparable values to previously published relationships (Mesarchaki et al., 2015). More recently, the same Aeolotron tank was used to determine the reducing effects of surfactants on gas transfer velocity at lower and higher wind speeds, based on a series of experiments conducted at wind speeds ranging from 1.5 to 22.8 m s^{-1}. Wind-wave tanks are particularly useful in studying gas exchange at high wind speeds, in which research vessels cannot safely operate. A wind-wave tank in Kyoto, Japan was used to study gas transfer

velocity at extreme wind speeds, up to 67.1 m s^{-1} using two organic tracers (Krall and Jähne, 2014). The result was largely in agreement with the only field study available at a similarly high wind speed, in which gas transfer velocities were measured using floats during a hurricane (McNeil and D'Asaro, 2007). However, one problem with wind-wave tank experiments is that the depth to which bubbles are injected is shallower than in the open ocean. For example, the SUrge STructure Atmosphere INteraction Facility (SUSTAIN) wind-wave tank, where the research for this thesis took place, is 2 m tall and the water depth used in our study was 0.75 m. Since bubble plume depths observed in the real ocean can reach depths of up to more than 20 m (Vagle et al., 2012; Vagle et al., 2010), we may not be able to directly transfer our results to make predictions in the ocean. Nonetheless, the relationship between gas flux and bubble size spectra, wind, and wave conditions learned from wind wave tank studies, such as the ones described above and the work presented in this thesis, provide us with valuable insights for improving global gas flux models.

1.6. Outline

The goal of my thesis project is to quantify air-sea gas exchange under high wind speeds and to examine the relationship between noble gas measurements, bubble distribution, wave-type, and water temperature. This thesis project is based on measurements collected at the SUSTAIN wind-wave tank where other Stanley lab members and I conducted a series of experiments in July 2018, in collaboration with members of the Haus lab at the University of Miami. Throughout the experiments with varying wind, wave, and water temperatures, we obtained measurements of discrete and continuous noble gases in conjunction with images of bubbles captured under water. The focus of this thesis will be on the treatment of the noble gas data, and their interpretation in relation to the bubble data under various physical conditions. In the remaining sections of this thesis, I describe the experimental setup and analysis techniques (Chapter 2, Methods), the mathematical treatment required to correct the continuous noble gas data (Chapter 3, Data Treatment), discrete and continuous noble gas data and insights in air-sea gas exchange gleaned from that data (Chapter 4, Results and Discussion), and suggestions for future directions (Chapter 5, Conclusions).

Chapter 2. Methods

2.1. Experimental overview

Over the period of July 10th to July 14th in 2018, we conducted 35 experiments with systematically varied water temperatures, wind speeds, and wave types in the SUSTAIN wind wave tank. Wind speeds were set to ranges over U_{10} = 20 - 50 m s^{-1} (steps of 5 m s^{-1}), water temperatures were set at 20°C, 26°C, and 32°C, and wave types were chosen to be either uniform waves (regularly breaking waves) or JONSWAP waves (random, real ocean-like waves). For the JONSWAP condition, an additional experiment was conducted with the wind speed at 10.6 m s^{-1}. The three temperatures were chosen to create environments in which the atmosphere is stable (20°C), neutral (26°C), or unstable (32°C) depending on whether the water is colder, similar, or warmer than the atmosphere. A summary of the experimental condition is presented in Table 1. The duration of each experiment ranged from about 40 - 85 minutes. This was so that we could observe the behavior of the noble gases and bubbles as they change from undergoing physical forcing to when they reach steady-state equilibrium. During the experiments, the SUSTAIN tank was filled with real ocean water from the local Biscayne Bay to a water depth of 0.75 m. Prior to filling the tank, the tank was first bleached with liquid pool bleach (16-gallons, 12.5% sodium hypochlorite by weight) and then was flushed with filtered seawater. This was to make sure that we eliminated contamination and to prevent biological consumption of O_2, a gas we also measured for gas exchange purposes. The salinity of the seawater ranged from 33.6 to 35.1 psu (practical salinity unit) over the course of the experiments.

Throughout the experiments, continuous and discrete noble gas measurements were obtained to study gas exchange, using the GEMS system and copper tube sampling method, respectively. The GEMS system provides continuous, real-time measurements of six noble gas ion current ratios: Ne/Xe, Kr/Xe, Ar/Kr, Ar/Xe, Ne/Kr, and Ne/Ar. In addition to the continuous noble gas measurements, discrete noble gas measurements were collected using the copper tube sampling method and were later processed by an in-lab mass spectrometer at the Isotope Geochemistry Facility at Woods Hole Oceanographic Institute (WHOI). In total, 55 discrete noble gas measurements were collected, and concentrations of He, Ne, Ar, Kr,

and Xe at the beginning of select experiments and at the end of all the experiments were obtained. In addition to the noble gases, bubble images were obtained by an underwater shadowgraph imaging device. The bubble imager provides us with the information about bubble size distribution and total volume occupied by the bubbles. Information on experimental set up as well as the continuous and discrete noble gas sampling are provided in detail in the subsequent sections of this chapter.

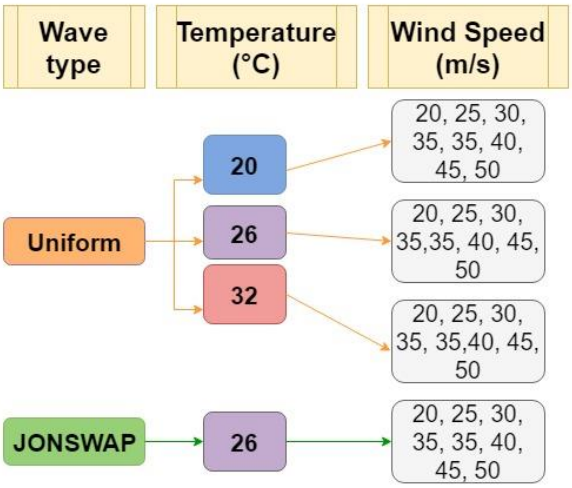

Figure 5. Summary of experimental conditions. For uniform and JONSWAP waves, a set of experiments were conducted for water temperatures 20°C, 26°C, and 32°C. Wind speeds ranged $U_{10} = 20$ - 50 m s^{-1} with 5 m s^{-1} increment (While not shown in the figure, JONSWAP wave had an additional 10.6 m s^{-1} run). *Figure credit: Danielle Aldrett '21 by personal communication.*

Exp. #	**Exp. day**	**Date**	**Start time**	**End time**	**Water temp (°C)**	**Wind speed at U_{10} (ms^{-1})**	**Wave type**	**Wave frequency (Hz)/ Peak period (sec)**	**Wave amplitude (m)**
Tank cooled down from around 32°C to 26°C									
1	One	7/10	15:39	16:52	26	35	uniform	1 Hz	0.15
2	One	7/10	18:52	19:58	26	20	uniform	1 Hz	0.15
3	One	7/10	21:38	23:03	26	25	uniform	1 Hz	0.15
4	One	7/11	2:43	3:26	26	40	uniform	1 Hz	0.15
5	One	7/11	4:44	5:18*	26	45	uniform	1 Hz	0.15
6	One	7/11	6:56^{+}	7:37*	26	50	uniform	1 Hz	0.15
7	Two	7/11	13:45^{+}	14:42*	26	30	uniform	1 Hz	0.15
8	Two	7/11	16:45	17:50*	26	35	uniform	1 Hz	0.15
Tank cooled down from 26°C to 20°C									
9	Two	7/11	20:02^{+}	21:07*	20	35	uniform	1 Hz	0.15
10	Two	7/11	23:10^{+}	0:05*	20	20	uniform	1 Hz	0.15
11	Two	7/12	2:26	3:17*	20	40	uniform	1 Hz	0.15
12	Two	7/12	4:32	5:20*	20	45	uniform	1 Hz	0.15
13	Two	7/12	6:30^{+}	7:11*	20	50	uniform	1 Hz	0.15
14	Three	7/12	13:40	14:58*	20	25	uniform	1 Hz	0.15

15	Three	7/12	16:15	16:57*	20	30	uniform	1 Hz	0.15
16	Three	7/12	17:48	18:31*	20	35	uniform	1 Hz	0.15
Tank warmed up from 20°C to 26°C									
17	Three	7/12	21:45^{+}	22:46*	26	35	uniform	1 Hz	0.15
Tank warmed up from 26 °C to 32 °C									
18	Three	7/13	1:08^{+}	1:48*	32	35	uniform	1 Hz	0.15
19	Three	7/13	2:43	3:24*	32	40	uniform	1 Hz	0.15
20	Three	7/13	4:57	5:32*	32	45	uniform	1 Hz	0.15
21	Three	7/13	6:32	7:09*	32	50	uniform	1 Hz	0.15
22	Four	7/13	13:58	14:55	32	20	uniform	1 Hz	0.15
23	Four	7/13	17:36	18:20*	32	25	uniform	1 Hz	0.15
24	Four	7/13	19:31^{+}	20:21*	32	30	uniform	1 Hz	0.15
Tank cooled down from 32°C to 26°C									
25	Four	7/13	22:55	23:33*	26	35	JONSWAP	0.65 sec	0.5
26	Four	7/14	3:01	3:44*	26	40	JONSWAP	1 sec	0.5
27	Four	7/14	4:55	5:30*	26	40	JONSWAP	1 sec	0.15
28	Four	7/14	6:35	7:08*	26	45	JONSWAP	1 sec	0.15
29	Four	7/14	7:53^{+}	8:24*	26	50	JONSWAP	1 sec	0.15
30	Five	7/14	14:33^{+}	15:39	26	10.6	JONSWAP	1 sec	0.15

31	Five	7/14	15:46	16:49	26	20	JONSWAP	1 sec	0.15
32	Five	7/14	17:43	18:31*	26	25	JONSWAP	1 sec	0.15
33	Five	7/14	19:25^{+}	20:10*	26	30	JONSWAP	1 sec	0.15
34	Five	7/14	20:56	21:39*	26	35	JONSWAP	1 sec	0.15
Tank warmed up from 26°C to 32°C									
35	Five	7/14	23:23^{+}	0:12*	32	20	uniform	1 Hz	0.15

Table 1. Detailed experimental conditions for the 35 experiments conducted with varying water temperatures, wind speeds, and wave types. Experiment start/end times are UMT time. ($^{+}$ indicates discrete samples were taken right before the winds and waves started, * indicates discrete samples were taken right after the winds and waves were stopped.)

2.2. Experimental set-ups

2.2.1. SUSTAIN tank

The SUSTAIN tank is the nation's largest wind-wave tank with dimensions 23 m long × 6 m wide × 2 m tall (76 ft × 20 ft × 7 ft) (Figure 6). It is covered with clear, acrylic walls framed in stainless steel, allowing visualization of conditions inside the tank. The SUSTAIN tank is equipped with a 1460 HP fan that can produce winds up to $U_{10} = 110$ m s^{-1}, equivalent to a category 5 hurricane. The SUSTAIN tank also has 12 wave paddles located at the end that can produce directional waves with specified wave amplitude and frequencies (Figure 7). The tank offers water temperature control and is designed for saltwater use (Alfred C. Glassell Jr. SUSTAIN Laboratory, 2015).

The Gas Equilibration Mass Spectrometer (GEMS) was put inside a wooden box placed above a platform anchored to the facility's ceiling (Figure 8). The crane rack running along the ceiling in which the platform was anchored to can be seen in Figure 6. By putting the mass spectrometer on a platform suspended from a crane, we hoped to reduce environmental noise by minimizing the stress from the tank's vibration and by creating a more temperature-controlled environment.

On the same platform as the GEMS, an Equilibration Inlet Mass Spectrometer (EIMS) was placed to measure O_2/Ar ratios. EIMS has a very similar set-up to GEMS but uses a Pfeiffer PrismaPlus quadrupole mass spectrometer and does not have the getters (Cassar et al., 2009) (Figure 9). A single acrylic panel directly under the platform at the center of the tank was removed to deliver water to the mass spectrometers located above the tank. The bubble imager was submerged under water and the water pump that delivers the water up to the mass spectrometers was placed at the same height to the bubble imager (Figure 10). Additionally, other equipment such as the optode, CTD (Conductivity Temperature Depth profiler), IRGASON, and vectrino were placed to measure water temperature, O_2 concentration, salinity, CO_2 concentration, atmospheric pressure, wind speed, and 3D water velocity fluctuations.

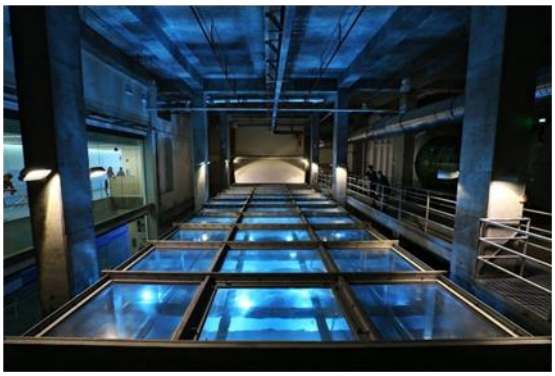

Figure 6. Overhead view of the SUSTAIN tank showing overhead space and acrylic construction. The wind generating fan is shown on the righthand side. Crane rack can be also seen running down the middle of the facility ceiling. *Photo credit: SUSTAIN Laboratory.*

Figure 7. Mechanically generated breaking wave captured from the side of the SUSTAIN tank. *Photo Credit: SUSTAIN Laboratory.*

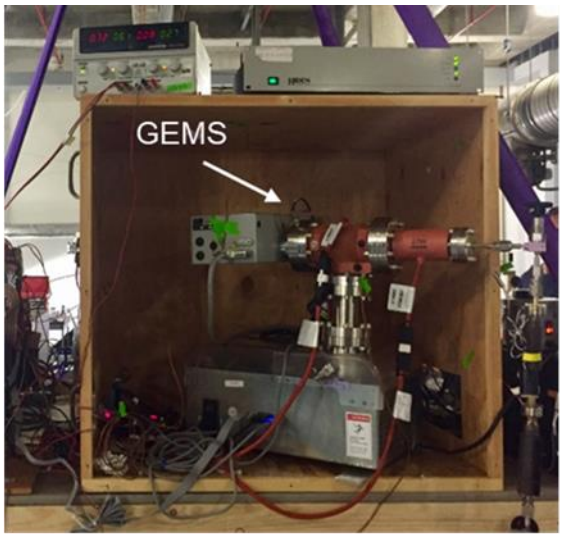

Figure 8. GEMS placed inside a wooden box placed on a platform anchored to the ceiling.

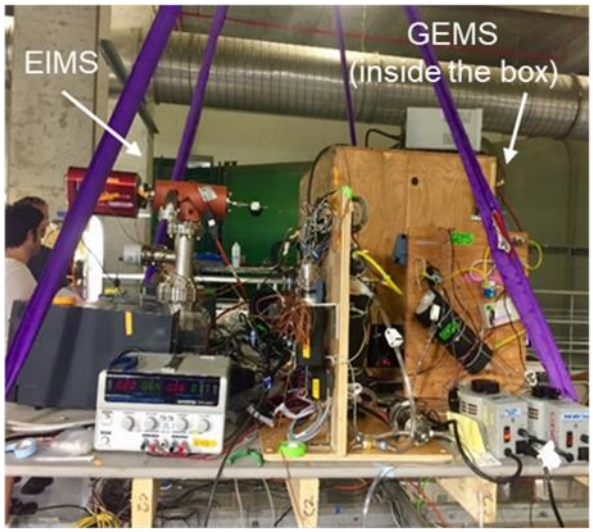

Figure 9. EIMS (left) and wooden box containing GEMS (right) on a platform suspended from the ceiling.

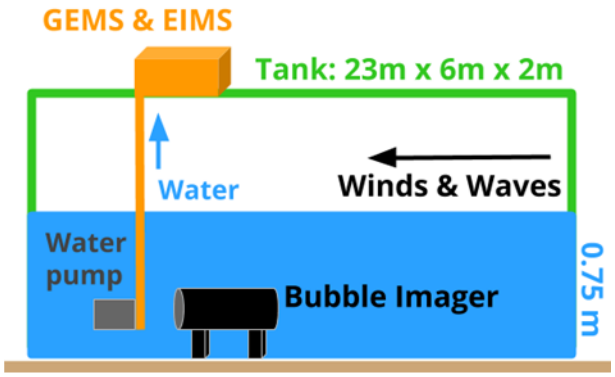

Figure 10. Side view of the SUSTAIN tank showing the placement of water pump, bubble imager, and the mass spectrometers. The bubble imager was placed closer to the direction of incoming winds and waves than the water pump delivering water to the mass spectrometers directly above it.

2.2.2. Water delivery and drainage system

Since the tank water had to be delivered to the mass spectrometers placed on top of the tank, a water delivery system was developed (Figure 11). Using a Smart Pond 500-Gph submersible fountain pump, water was first pumped through a 3/4" ID × 1" OD clear vinyl tubing into a 5-L Nalgene beaker. The Nalgene beaker was the innermost layer of the bucket

system and was suspended inside a 3-gallon plastic bucket. From the Nalgene beaker, the water sample was delivered to GEMS and EIMS via flexible 3/8" OD × 1/4" ID PVC tubes after going through two layers of filters—a filter bag and then a filter sock to remove contamination in the water. The polyester filter bag had 25 um pore size with dimensions 5.5" OD × 15" long. The filter sock was 2-layered, with 5 mm inner x 100 mm outer pore size and dimensions 12" long × 1.5" wide. Holes were drilled radially, approximately two inches from the top of the Nalgene beaker, to allow the water to flow out once it reaches a certain level. The outermost container of the bucket system was a 10-gallon plastic bin with a draining hole connected to a 3/4" ID × 1" OD clear vinyl tubing to deliver water back to the tank. Inside the plastic bin, an additional submersible pump was placed inside the bin to prevent water from overflowing. Once the water was equilibrated for measurement, it was returned back into the tank from the opposite end of the wave paddles, away from the instruments and sensors to prevent interference with measurement conditions. Additionally, insulating foam was placed along the PVC tube that stretched to the drainage site to prevent changes in water temperature from being exposed to the atmosphere.

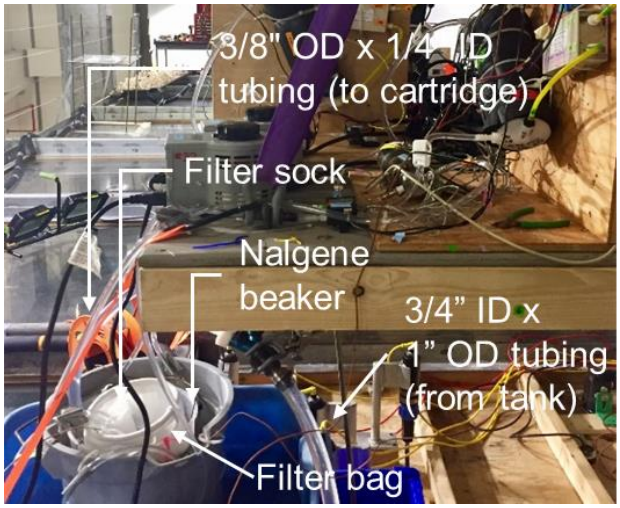

Figure 11. Picture of the water delivery system. The water was brought to the top of the tank through a 3/4" ID × 1" OD tubing to the Nalgene beaker. From the Nalgene beaker, the water was delivered to the GEMS and EIMS equilibration cartridge through 3/8" OD × 1/4" ID tubing, which was placed inside two layers of filters (filter sock and filter bag) inside the Nalgene beaker.

2.3. Gas Equilibration Mass Spectrometer (GEMS)

The dissolved noble gas ratios (Ne/Xe, Kr/Xe, Ar/Kr, Ar/Xe, Ne/Kr, and Ne/Ar) were obtained using a recently developed field deployable Gas Equilibration Mass Spectrometer (GEMS) (Manning et al., 2016). GEMS cannot measure He because He is

permeable to the system due to its silica-based capillary. GEMS can be transported easily, costs significantly less, and provides real-time noble gas measurements unlike traditional in-lab mass spectrometers. Additionally, previous testing in the laboratory has shown that GEMS has an accuracy 0.9% or better for all gas ratios when calibrated with air, and the accuracy improves to 0.6% or better when calibrated with discrete samples (Manning et al., 2016). The e-folding time, or τ, where roughly 63% of the gas becomes equilibrated, ranges from 1.5 to 7 minutes depending on the gas, where Xe is the fastest and Ne is the slowest to equilibrate. In our experiment, GEMS measured dissolved noble gas when the experiment was running; when the experiment was not running, GEMS was measuring noble gases in the air for calibration. The temporal resolution for GEMS was approximately 60 seconds.

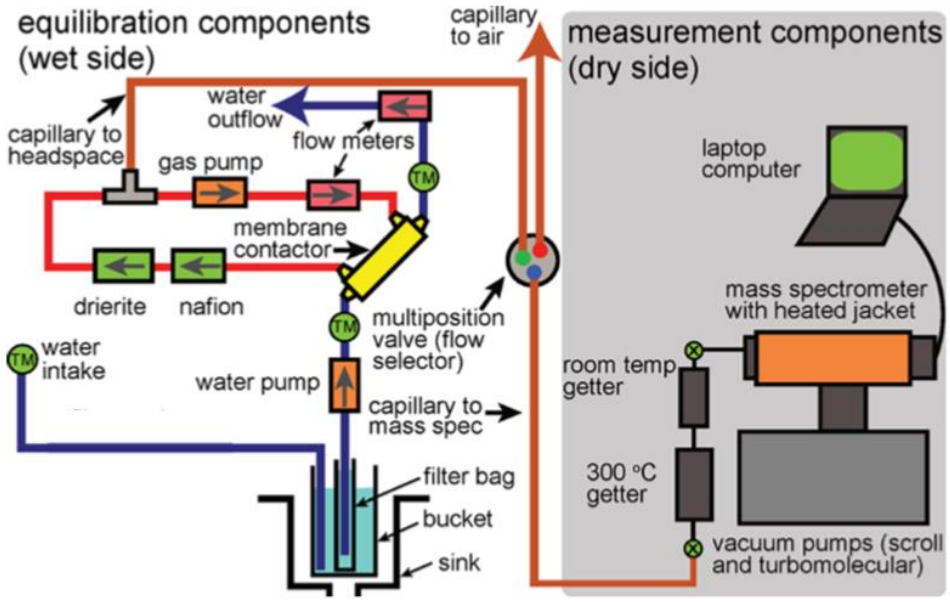

Figure 12. Schematic of Gas Equilibration Mass Spectrometer (GEMS) instrumental set-up. GEMS system can be divided into equilibration and measurement components. Figure adapted from Manning et al. (2016). Not drawn to scale.

The GEMS system can be divided into the equilibration (wet side) and the measurement (dry side) components (Figure 12). In the equilibration components, the filtered water sample is drawn into the membrane contractor cartridge. Inside the membrane contractor cartridge, the dissolved gas is equilibrated with the air in the headspace, and the

equilibrated air is dried and fed into the capillary, which eventually leads to the quadrupole mass spectrometer. The key feature of this system is that the gases dissolved in the water sample flowing through the membrane contractor must be in equilibrium with the gases in the headspace. To ensure this, the air in the headspace is continuously recirculated in the opposite direction to the water pathway. The air exiting the headspace is dehydrated by using two drying agents, molecular sieves and Drierite, to maximize the mass spectrometer signal for noble gases. The equilibrated air also contains undesired gases prevalent in the environment, such as CH_4, N_2, and H_2, in addition to water vapor.

In the measurement components, unwanted gases (N_2, O_2, CH_4, H_2, etc.) are removed by the two getters placed in-line of the capillary pathway, right before the air enters the mass spectrometer. The first getter breaks the C-H bond in the CH_4, and the second getter absorbs H_2, and both getters remove all other gases except for the noble gases. In addition to the gases dissolved in the water sample, the mass spectrometer also measures gases in the atmosphere for calibration using a capillary open to the air. Since gases in both the water sample and the air cannot be measured at exactly the same time, the desired flow is selected using a multi-position valve. In Figure 12, the multi-position valve (flow selector) can be found with the valve connecting the capillary from the water sample shown in green and the valve connecting the capillary from the air shown in red. The valve connecting the capillary to the mass spectrometer (blue) is always open. It is important to note that, GEMS is used to obtain molar ratios, rather than concentrations. This is because the amount of gases flowing through the capillaries in air and headspace differ by a few percent, which limits us from using the known noble gas concentrations in air as our "true" value to derive the actual noble gas concentrations in the water sample (Manning et al., 2016). While GEMS doesn't provide the absolute concentration of each gas, saturation anomaly can be calculated using molar ratios as shown in Equation 5. Similar to Equation 4, the saturation anomaly for gas ratio is a measure of the direction and degree of departure away from equilibrium.

$$\Delta\frac{\mathrm{Ne}}{\mathrm{Xe}} = \left(\frac{\left[\frac{\mathrm{Ne}}{\mathrm{Xe}}\right]\mathrm{water}}{\left[\frac{\mathrm{Ne}}{\mathrm{Xe}}\right]\mathrm{equil}} - 1\right) * 100. \qquad \text{(eq 5)}$$

A detailed description of how the GEMS data was processed is in Chapter 3 of this thesis.

Shortened lists of the GEMS instrumentation are provided for measurement component (Table 2) and equilibration component (Table 3). The complete list of components can be found in Tables S3 and S4 in Manning et al., 2016.

Description	Supplier/Part #	Function
Quadrupole mass spectrometer with triple mass filter, Faraday and SCEM detectors, 1 - 200 amu range	Hiden Analytical/HAL 3F RC201, 553010/200	Noble gas detection
Quadrupole mass spectrometer ion source control module	Hiden Analytical/304800	Noble gas ionization
Vacuum pumping station (TPS-Compact with Turbo-V 301 Navigator turbomolecular and IDP-3 dry scroll pump)	Agilent/X3580A#011#024#120	Create vacuum inside QMS
Manifold/housing for quadrupole	Sharon Vacuum/custom	Housing for QMS
Heating jacket with adjustable set-point and display module	MKS/custom, from series 48	Maintains the temperature inside QMS
St2002 getter, cylindrical pieces, 6 mm diameter, 2 mm long	SAES Getters/5F0542	Remove other gases
Uninterruptible power supply (UPS) and power conditioner	Eaton/PW9130L-1000T-XL	Power supply

Table 2. Abbreviated list of measurement components, their descriptions, suppliers, and functions. A complete list can be found in Table S3 in Manning et al. (2016).

Description	Supplier/Part #	Function
Membrane contactor, Extra-Flow 2.5 x 8, X40 fiber	Membrana Liqui-Cel/ G420	Equilibrates dissolved gas with air
Nafion dessicant box	PermaPure/ DM-110-24	Dry circulating gas
Micro diaphragm pump	Parker/Hargraves Fluidics/ E191-11-060	Circulate gas
Water pump head, A-mount suction shoe, 1.17 mL/rev	Cole-Parmer/Micropump/ EW-07003-04	Circulate water
Water pump drive, 150 - 4000 rpm	Cole-Parmer/Micropump EW-07003-90	Circulate water
Felt filter socks, 2-layer, 5 mm inner, 100 mm outer pore size, 12” long x 1.5” wide	Universal Filters PG5/100-1.5FX12	Prevent membrane clogging
Polyester filter bag, 25 um pore size, 5.5” OD x 15” long	Filter Source PES25P7PPH	Prevent membrane clogging
Deactivated fused silica capillary, 0.05 mm ID, 0.36 mm OD	Agilent/160-2655-10	Measuring inlet
Valco multi-position valve with flow selector	VICI Valco/C5-1306EMH2Y	Allow switching between air and water measurements
flexible PVC tubing, 1/4” ID x 3/8” OD	McMaster-Carr/5233K56	Water pathway
flexible PVC tubing, 1/8” ID x 1/4” OD	McMaster-Carr/5233K52	Gas pathway

Table 3. Abbreviated list of equilibration components, their descriptions, suppliers, and functions. A complete list can be found in Table S4 in Manning et al. (2016).

2.4. Discrete noble gas samples

In addition to the GEMS continuous noble gas measurements, we also obtained discrete noble gas samples for He, Ne, Ar, Kr, and Xe at the beginning of select experiments and at the end of all the experiments. In total, 58 copper tube samples were analyzed, including 6 duplicate samples (see Table 10 in Results chapter). The duplicate sample points were later averaged, resulting in 53 total discrete noble gas sample points. The purpose of collecting the discrete noble gas data was to obtain accurate noble gas concentrations since GEMS only provides the information on mole ratio, rather than concentration. In addition to providing information about He and its isotope ^{3}He which are permeable to GEMS, the concentration data from the discrete noble gas sample are also useful in running gas exchange models and to calculate gas flux. Finally, the discrete noble gas data were used to calibrate the GEMS noble gas data, for which a detailed explanation is provided in the subsequent chapter on data treatment.

The discrete noble gas samples were collected using the copper tube sampling method, which keeps the water sample in a tightly sealed environment until the gases are extracted in lab right before analysis (Spitzer and Jenkins, 1989; Weiss, 1968). The samples were then shipped to Isotope Geochemistry Facility at WHOI and analyzed by an in-lab mass spectrometer capable of measuring noble gas concentrations with 0.2% or better precision. The mass spectrometer purifies the noble gas sample with a water vapor trap, Pd catalyst, and two getters, followed by either the charcoal cryogenic trap (separates He) or stainless-steel cryogenic trap (separates Ne, Ar, Kr, and Xe) (Stanley et al., 2009a). The samples are then analyzed by a quadrupole mass spectrometry and by magnetic sector mass spectrometry to determine the abundance of each noble gas.

2.5. Ancillary measurements

In addition to the noble gases, other physical measurements were also obtained during our experiments. A bubble imager was submerged under water and an optode was fixed onto a mast by the location of water intake for the mass spectrometers (Figure 13). The bubble imager enables us to visualize bubbles as shadows using the shadowgraph technique.

The bubble imager provided us with information on bubble size distributions and void fraction. It uses two Fresnel lenses to collimate the LED light, which decreases the dependency of the detected bubble sizes on the distance of the bubbles from the light source. The frequency of the bubble image taken was 5 Hz and the observable range of the bubble radii were between 30 um and 1.5 mm. The dimensions of the volume captured by the bubble imager were 51.471 mm (in X or along-tank) × 68.471 mm (in Z or depth) × 100.000 mm (in Y or across-tank) which equals to 3.5242×10^{-4} m^3. The center of the bubble imager volume was 45 cm from the bottom of the tank, and the depth range observed by the bubble imager account was approximately Z = 42 - 48 cm. The optode used in this study was Aanderaa oxygen optode, which obtained continuous O_2 concentration and water temperature measurements.

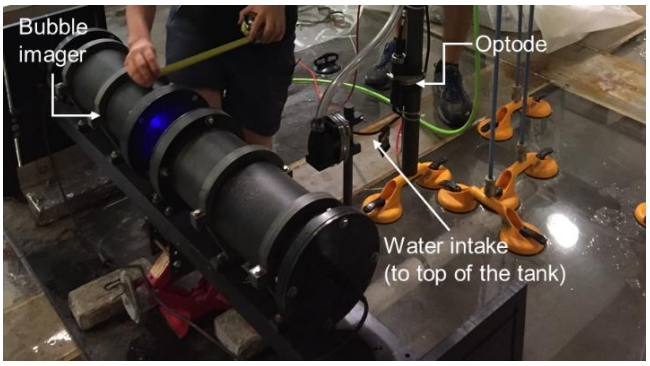

Figure 13. Picture of the bubble imager, water pump, and optode from when the instruments were being set up (the tank was not yet filled with water).

The bubble imager, water pump, and optode were placed in that order with the bubble imager being closest to the end of the tank where the winds and waves were generated, to make sure that the bubble images were undisturbed (Figures 14 and 15). In addition, continuous salinity measurement in different locations in the tank was taken by the CTDs. Interpolated discrete salinity measurement data (n=22) and water temperature measurement taken from the optode were used to calculate the discrete noble gas saturation anomalies. Finally, a polarimetric camera and IR camera were used to measure wave properties (2D surface temperature of the air-water interface and 2D slope of the air-water interface, respectively), Nortek Vectrino 3D doppler current profiler was used to measure water velocity, and IRGASON was used to measure air temperature, atmospheric pressure, CO_2, H_2O, and

continuous wind velocities.

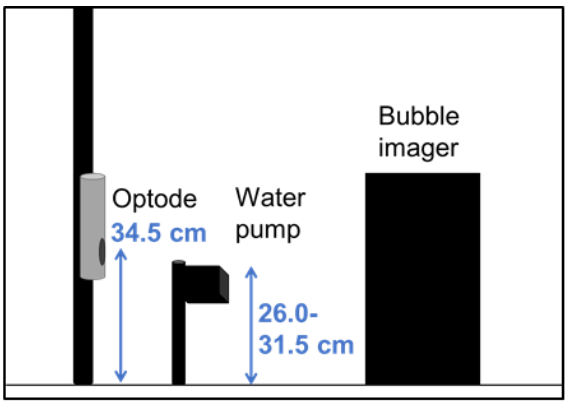

Figure 14. Side view of the relative positioning of optode, water pump, and the bubble imager. The heights of the optode sensor, the water intake, and the center of the bubble imager were adjusted be the same as one another. The winds and waves originated from the right-hand side of the bubble imager.

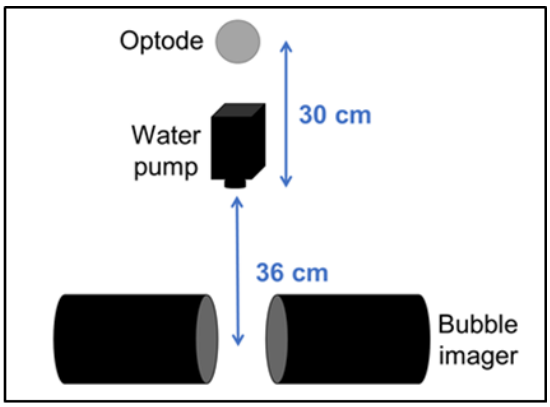

Figure 15. Top view of the relative positioning of the instruments. The water intake of was 36 cm away from the bubble imager and the sensor of the optode was 30 cm away from the water pump.

Chapter 3. Data Treatment

The GEMS continuous noble gas data was corrected for the (1) effect of temperature drift on the mass spectrometer and (2) for differences between the GEMS ratios and the corresponding discrete noble data. The two corrections methods applied to the GEMS continuous data and the rationales behind that led to the choice of a particular correction are explained in this section. These corrections are similar to those done by Callan Krevanko '18, a former member of the Stanley lab, who analyzed data from experiments conducted at the SUSTAIN the previous summer (Krevanko, 2018). The major difference between the previous year's correction method and that employed in this thesis is that cost functions were used to explore the variable times for temperature slope and averaging time window for the discrete data. A more detailed description is discussed in the following sections.

3.1. Temperature correction

GEMS continuous ion current ratio data must be calibrated for environmental effects

on the mass spectrometer, such as drift due to temperature change. To correct for the temperature-dependent signal change, we ran the mass spectrometer after all the experiments were conducted for each day and measured noble gases in air (i.e., mass spec was run "overnight"). The overnight data allows us to correct for the environmental effects since the change in ion current ratio of air can be assumed to be due to non-experimental effects. To correct for the effect due to temperature drift, the overnight ion current ratio was first plotted as a function of the air temperature for each of the five days and a best fit linear slope (correction slope) was calculated. An example of the overnight temperature data for Day 1 is shown in Figure 16. In the figure, the correction slopes are calculated for 2 - 62 minutes of the overnight ion current ratios in air plotted as a function of temperature. For all five days, the minimum temperature cut-off was set to be 28°C to avoid over-correcting the data, since the daytime temperature did not drop below 28°C over the course of experiments. In other words, even if the datapoint fell within the selected time duration, if the temperature taken at the corresponding time point was below 28°C, the datapoint was not included in slope calculation.

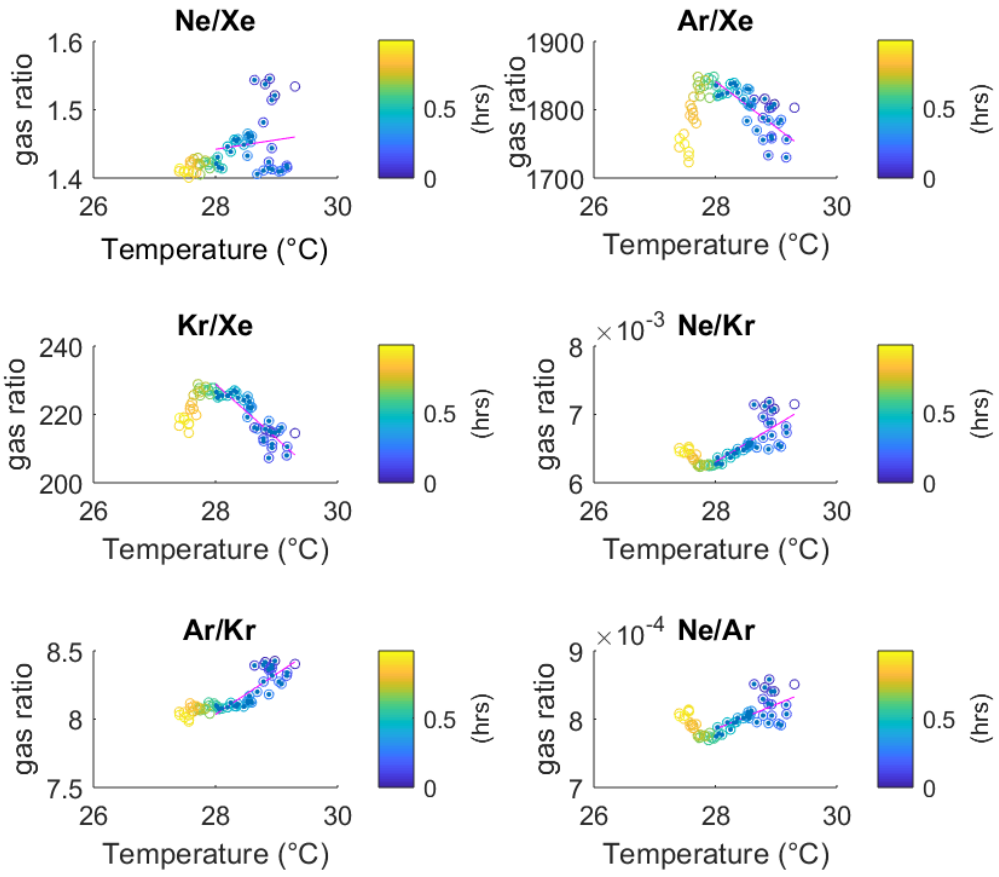

Figure 16. Overnight GEMS noble gas ratio data plotted against temperature for Day 1. The duration of the GEMS data in which the linear regression was calculated was 2 - 60 minutes after the air measurement started. The color bar represents the time elapsed since the first measurement in air that evening. Minimum temperature was set to 28°C for the correction slope calculation.

The caveat here is that the correction slopes depend on the range of selected overnight data and hence our choice of time period. We did not want to use all the overnight data since the mass spectrometer can drift for reasons other than temperature over time and we were trying to isolate the temperature effect. The air temperature changed most dramatically in approximately the first hour and thus we considered times near the beginning of each night. To choose the most appropriate temperature correction, an optimization calculation was conducted. As a first step, three different correction slopes were generated with varying start and end time in which the overnight ion current data were selected (Table 4). The start time was selected to be 2 minutes and 5 minutes, so it is within the range of the

GEMS e-folding time of 1.5 to 7 minutes (Manning et al., 2016). This ensures that the GEMS system has had enough time to equilibrate with the ambient air after the experiments were completed. The end time were set to 60 minutes (slope 1 and 2) and 45 minutes (slope 3) to cover the linear range of the data.

Correction slopes	**Start time** (time elapsed since last switch to air)	**End time** (time elapsed since last switch to air)
Slope 1	2 minutes	62 minutes
Slope 2	5 minutes	65 minutes
Slope 3	5 minutes	50 minutes

Table 4. Selected time windows for the three correction slopes.

A compilation of the correction slopes for each noble gas ratios is listed in Table 5. For Days 1 - 3, correction slopes 2 and 3 are identical because they both have the same starting time, and the end point was selected based on temperature cut off at 28°C rather than their respective end times. Once the correction slopes were calculated, they were applied to the daytime raw ion current data using the following equation:

$$\text{gas ratio}_{\text{new}} = \text{slope} * (28°\text{C} - \text{temperature}) + \text{gas ratio}_{\text{original}}. \quad \text{(eq 6)}$$

The correction slopes were then applied to the daytime noble gas ion current data from that day. For example, correction slope for Day 1 was applied to correct the daytime ion current gas ratios for Day 1. We chose to apply daily correction slopes for each day, rather than the averaged correction slopes across five days, to account for the difference in day-to-day mass spectrometer temperature response. If the drift was solely accounted for the effect of temperature, the slopes should theoretically be the same across different days, given that the change in temperature over the time period of interest was approximately between 28°C to 30°C. This was not the case, however, as slopes differ largely across different days for each ratio. This may be due to the change in the temperature and air composition of the SUSTAIN tank facility due to the differences in the experiments conducted during the day.

	Ne/Xe	Ar/Xe	Kr/Xe	Ne/Kr	Ar/Kr	Ne/Ar
Day 1						
Slope 1	0.014	-67	-16.0	0.00054	0.300	3.6E-05
Slope 2	0.010	-72	-16.2	0.00052	0.281	3.5E-05
Slope 3	0.010	-72	-16.2	0.00052	0.281	3.5E-05
Day 2						
Slope 1	0.058	59	4.5	0.00013	0.106	4.8E-06
Slope 2	0.094	104	10.7	0.00009	0.069	3.3E-06
Slope 3	0.094	104	10.7	0.00009	0.069	3.3E-06
Day 3						
Slope 1	0.012	-78	-20.7	0.00063	0.397	4.01E-05
Slope 2	0.014	-60	-17.8	0.00054	0.363	3.29E-05
Slope 3	0.014	-60	-17.8	0.00054	0.363	3.29E-05
Day 4						
Slope 1	0.0064	-2.9	-5.4	0.000220	0.212	5.4E-06
Slope 2	0.0013	4.3	-4.1	0.000149	0.194	-1.4E-06
Slope 3	0.0116	-8.5	-5.0	0.000230	0.167	1.12E-05
Day 5						
Slope 1	0.0282	42.4	-0.48	0.000150	0.2235	-3.6E-06
Slope 2	0.0261	40.7	-0.26	0.000133	0.2070	-4.0E-06
Slope 3	0.0194	38.7	-0.25	9.9E-05	0.1967	-7.2E-06

Table 5. Three different correction slopes were calculated for each of the noble gas ratios for five days. Slopes were calculated using ion current ratios on the y-axis and temperature on the x-axis, with minimum temperature set to 28°C.

Finally, in order to choose the best slope, the temperature corrected GEMS saturation anomaly ratios were compared with the saturation anomaly ratios obtained from the discrete noble gas. The slope that yields the least difference from the "true" saturation anomaly obtained from the discrete noble gas was considered be the best correction slope. To do this, a single corresponding GEMS continuous value was obtained after the temperature correction for each of the discrete noble gas data point, by averaging over some time period after the discrete noble gas data was taken. For the averaging duration we chose either 5 or 10 minutes, ensuring enough time for GEMS to equilibrate the same water source that was used for the discrete measurement. A cost function based on the difference between the GEMS and discrete noble gas saturation anomaly ratio was then calculated using the following equation for each slope and ratio across the five days:

$$\text{cost function} = (\text{sat. anomaly ratio}_{\text{GEMS}} - \text{sat. anomaly ratio}_{\text{discrete}})^2. \quad \text{(eq 7)}$$

The compilation of the cost function for all five days are listed in Tables 6 and 7.

Cost Function (5 mins)	Ne/Xe	Ar/Xe	Kr/Xe	Ne/Kr	Ar/Kr	Ne/Ar	Sum
slope1day1	0.012	0.010	0.016	0.034	0.0059	0.012	0.090
slope2day1	0.011	0.010	0.016	0.033	0.0059	0.012	0.088
slope3day1	0.011	0.010	0.016	0.033	0.0059	0.012	0.088
slope1day2	0.037	0.035	0.054	0.011	0.0034	0.0043	0.145
slope2day2	0.047	0.046	0.068	0.012	0.0038	0.0043	0.180
slope3day2	0.047	0.046	0.068	0.012	0.0038	0.0043	0.180
slope1day3	0.012	0.013	0.018	0.029	0.0054	0.0079	0.086
slope2day3	0.012	0.013	0.018	0.030	0.0054	0.0083	0.087
slope3day3	0.012	0.013	0.018	0.030	0.0054	0.0083	0.087
slope1day4	0.0011	0.0028	0.0067	0.0120	0.0022	0.0042	0.0289
slope2day4	0.0011	0.0031	0.0073	0.0122	0.0021	0.0046	0.0304
slope3day4	0.0012	0.0025	0.0069	0.0120	0.0021	0.0040	0.0287
slope1day5	0.0029	0.0028	0.0034	0.0032	0.00089	0.00087	0.0140
slope2day5	0.0028	0.0027	0.0034	0.0031	0.00088	0.00087	0.0138
slope3day5	0.0026	0.0027	0.0034	0.0030	0.00087	0.00084	0.0135

Table 6. Cost function for the noble gas ratios for each day and slope when GEMS average was taken over 5 minutes after the corresponding discrete noble gas sample point. The cells highlighted in yellow represent the choice of slope(s) that yielded the smallest digression from the discrete noble gas sample point.

Cost Function (10 mins)	Ne/Xe	Ar/Xe	Kr/Xe	Ne/Kr	Ar/Kr	Ne/Ar	Sum
slope1day1	0.013	0.010	0.015	0.031	0.006	0.010	0.085
slope2day1	0.012	0.010	0.015	0.030	0.006	0.010	0.082
slope3day1	0.012	0.010	0.015	0.030	0.006	0.010	0.082
slope1day2	0.036	0.030	0.048	0.009	0.004	0.004	0.130
slope2day2	0.044	0.038	0.060	0.010	0.004	0.004	0.160
slope3day2	0.044	0.038	0.060	0.010	0.004	0.004	0.160
slope1day3	0.011	0.012	0.016	0.025	0.005	0.007	0.076
slope2day3	0.011	0.012	0.016	0.026	0.005	0.007	0.077
slope3day3	0.011	0.012	0.016	0.026	0.005	0.007	0.077
slope1day4	0.0013	0.0029	0.0071	0.0112	0.0023	0.0036	0.0283
slope2day4	0.0012	0.0032	0.0076	0.0114	0.0023	0.0039	0.0296
slope3day4	0.0014	0.0026	0.0073	0.0112	0.0023	0.0034	0.0282
slope1day5	0.0032	0.0033	0.0034	0.0033	0.0010	0.0010	0.0151
slope2day5	0.0031	0.0032	0.0035	0.0033	0.0010	0.0010	0.0151
slope3day5	0.0029	0.0032	0.0035	0.0033	0.0010	0.0010	0.0148

Table 7. Cost function for the noble gas ratios for each day and slope when GEMS average was taken over 10 minutes after the corresponding discrete noble gas sample point. The cells highlighted in yellow represent the choice of slope(s) that yielded the least digression from the discrete noble gas sample point.

Based on the cost function calculation, the best combination was found to be correction slope 3 and GEMS average duration of 10 minutes. The sum of all minimum cost functions for each day was 0.361 for 5 minutes GEMS average and 0.332 for 10 minutes GEMS average. For both durations, correction slope 3 yielded the minimum cost function for three out of five days and the sum of the minimum cost function for slope 3 alone was 0.130 for 5 minutes GEMS average duration and 0.126 for 10 minutes GEMS average duration. The cost function calculation for Day 2 is higher compared to other days, possibly because the GEMS vici valve was accidentally placed in air instead of water for a short period of time at the beginning of the Day's measurement. Otherwise, it is interesting to see that the GEMS noble gas data increasingly agrees with the discrete noble gas data as we progress from Day 1 to Day 5. Additionally, with the exception of Day 2, the differences in the sum of cost functions yielded from different slopes are within 5%, which reassures us that the choice of slope in a given day does not result in drastic difference in the temperature

correction. The temperature corrected saturation anomaly using correction slope 3 was plotted over the GEMS raw saturation anomaly data (Figure 17).

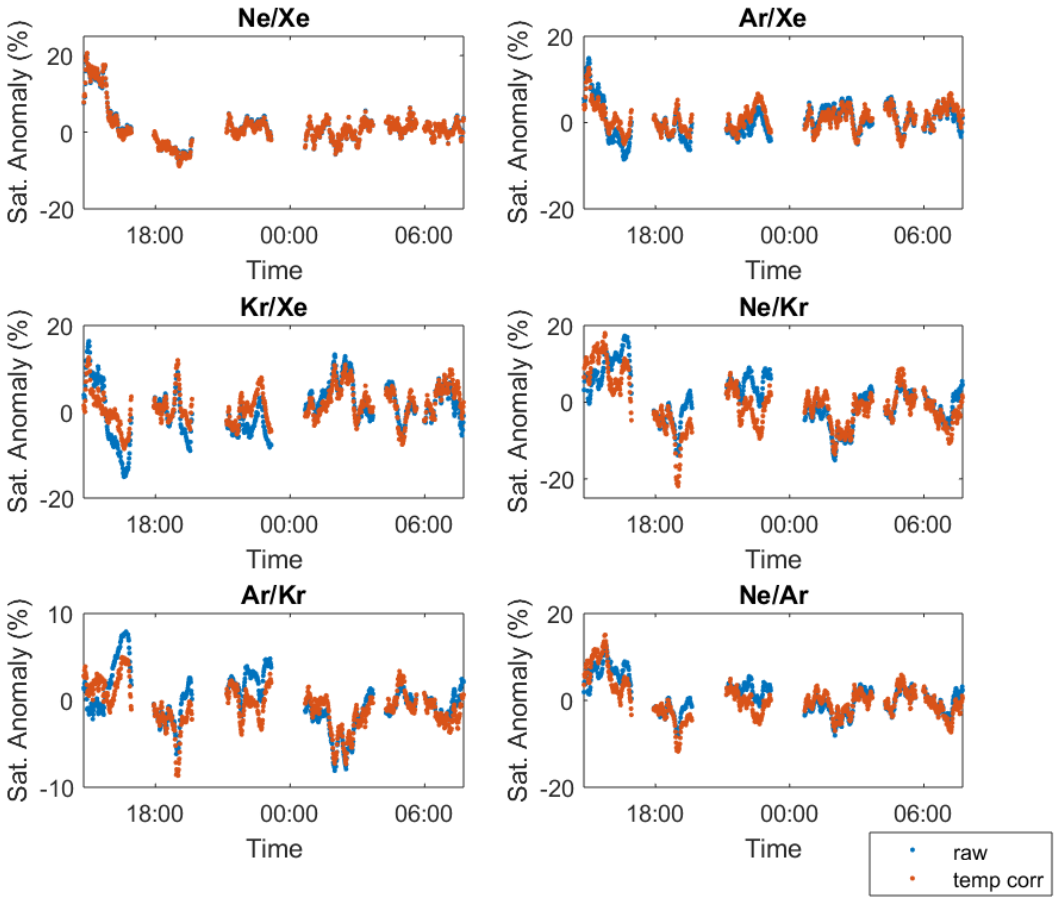

Figure 17. Raw and temperature corrected saturation anomaly for Day 1 (experiments 1-6). The temperature corrected GEMS saturation anomaly (orange) was plotted over the raw saturation anomaly (blue).

3.2. Discrete sample correction

After the temperature correction, another correction was made using discrete noble gas data. In order to do so, we calculated the "correction factor", which equals the averaged GEMS saturation anomaly ratio divided by the discrete saturation anomaly ratio. The correction factor can tell us about the magnitude of the difference between the GEMS continuous and discrete noble gas data. The smaller the necessary correction, the closer the correction factor value is to one. Then we calculated a linear regression of the correction

factor plotted against the GEMS saturation anomaly ratio size because there was a strong linear dependence between the correction factor and GEMS ratio size (Figure 18). We used this linear regression to calculate an appropriate cost function for every time point based on the GEMS gas ratios. We then applied these calculated correction factors to the temperature corrected GEMS continuous data. The corrected GEMS continuous data using the linear regression slope for Day 1 is shown in Figure 19.

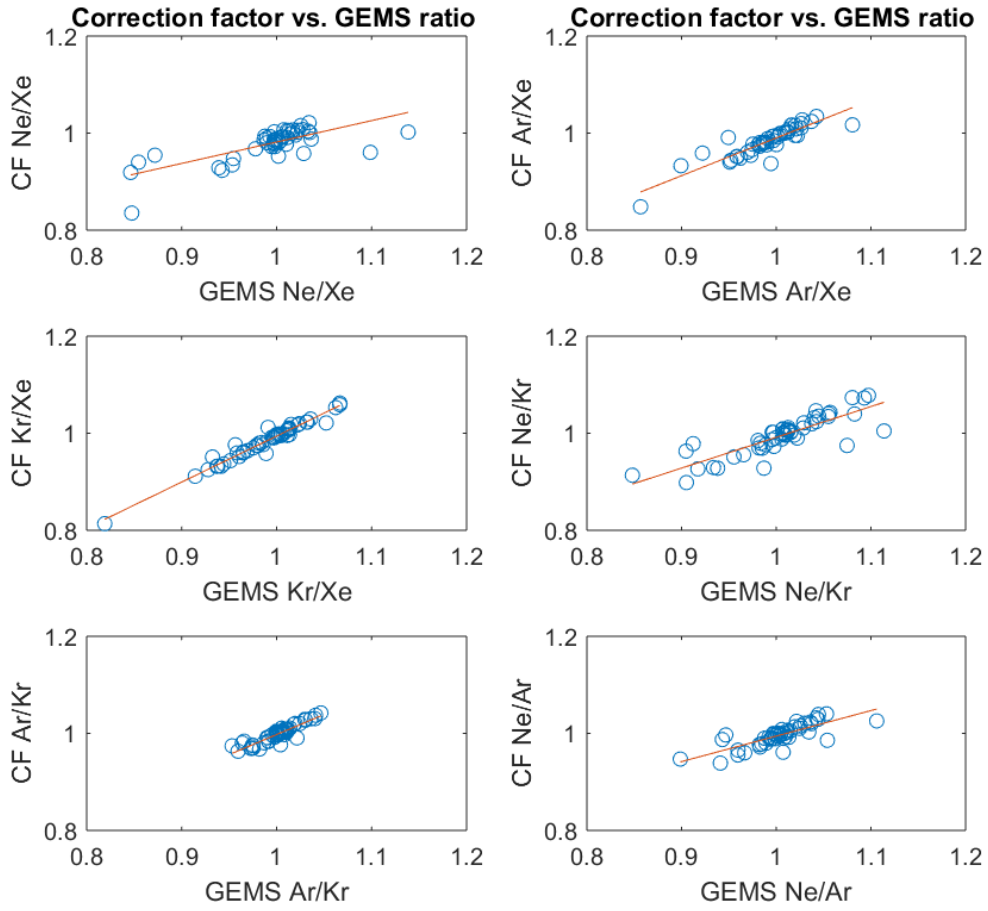

Figure 18. Correction factor was plotted as a function of all GEMS single value ratio size for each of the six noble gas ratios. The GEMS value was averaged for the duration of 10 minutes after the corresponding discrete noble gas sample was taken. There is a strong positive linear relationship between the correction factor and GEMS signal size. The red lines represent the slopes used in correcting the GEMS continuous data.

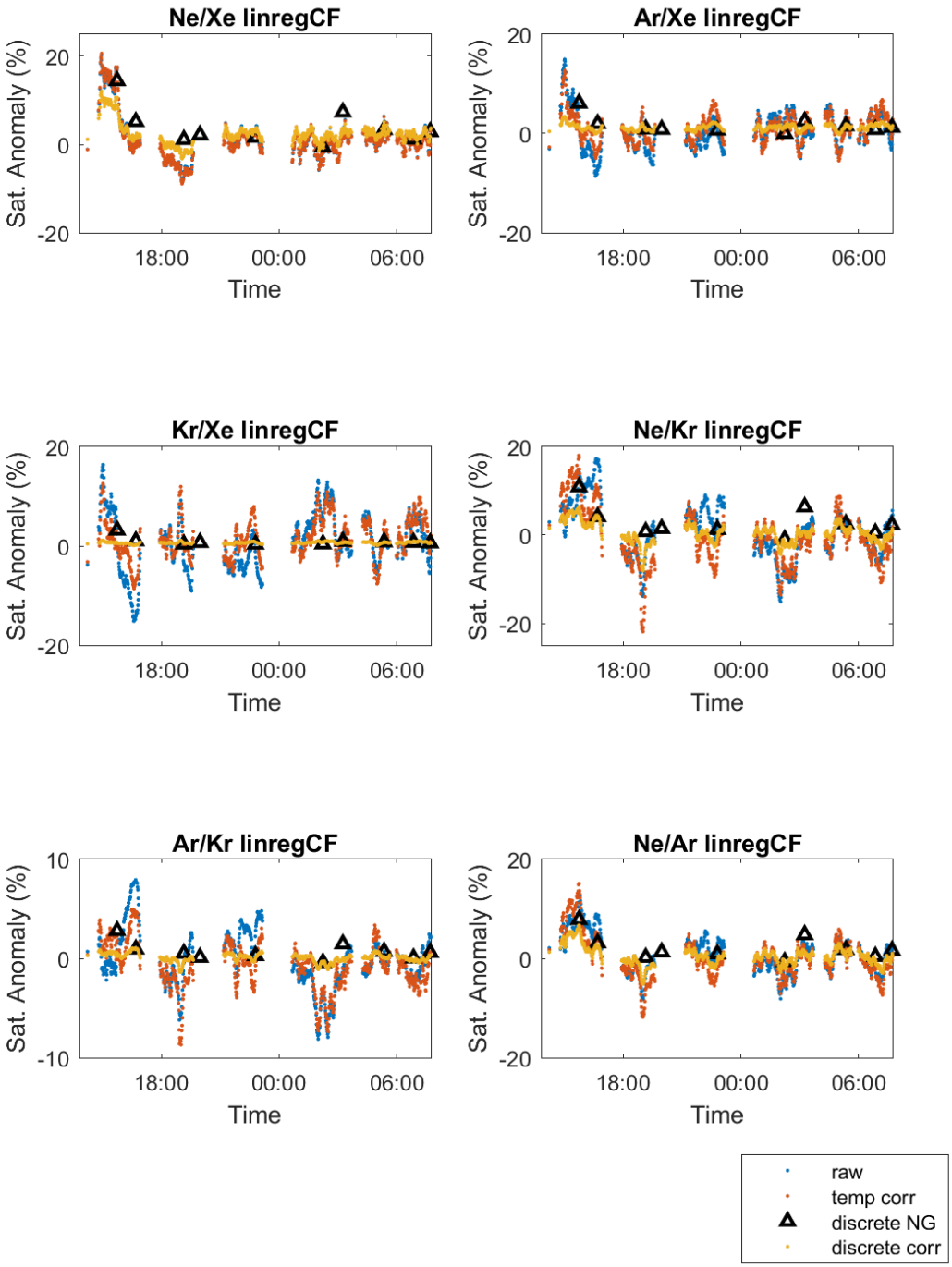

Figure 19. Temperature corrected GEMS continuous noble gas ratio was corrected by linear regression correction factor for Day 1 (experiments 1-6). The plot includes raw GEMS saturation anomaly data (blue), temperature corrected data (orange), discrete noble gas results (black triangles), and discrete noble gas corrected data (yellow). Significant signal flattening are observed for some of the ratios.

In doing the discrete noble gas correction, we considered using a daily average of the correction factor for each day, instead of the linear regression correction factor (Figure 20). Figure 21 shows the daily average correction factor applied to the GEMS continuous data for Day 1.

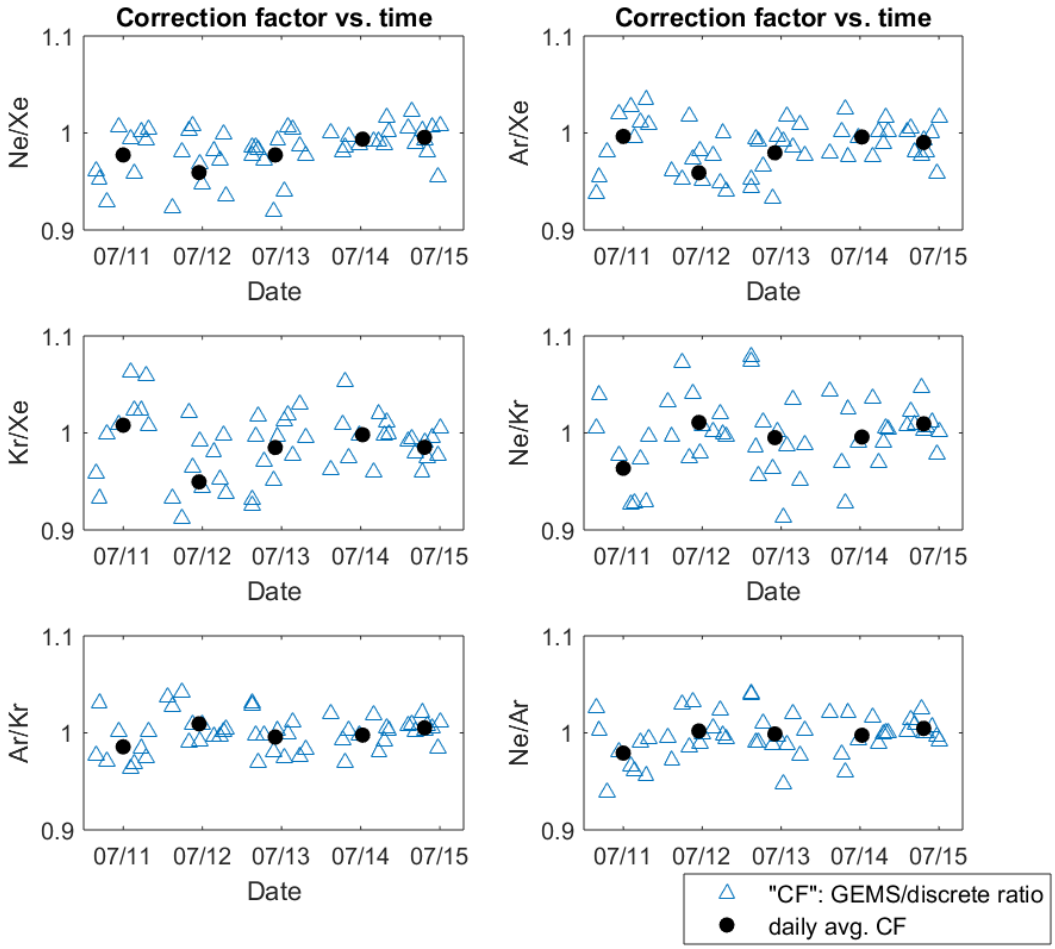

Figure 20. Correction factor was plotted and along with the average correction factor for each day for all six noble gas ratios. Blue triangles represent all the correction factors and the black circles represent the averaged correction factor for each experiment Day 1 through 5.

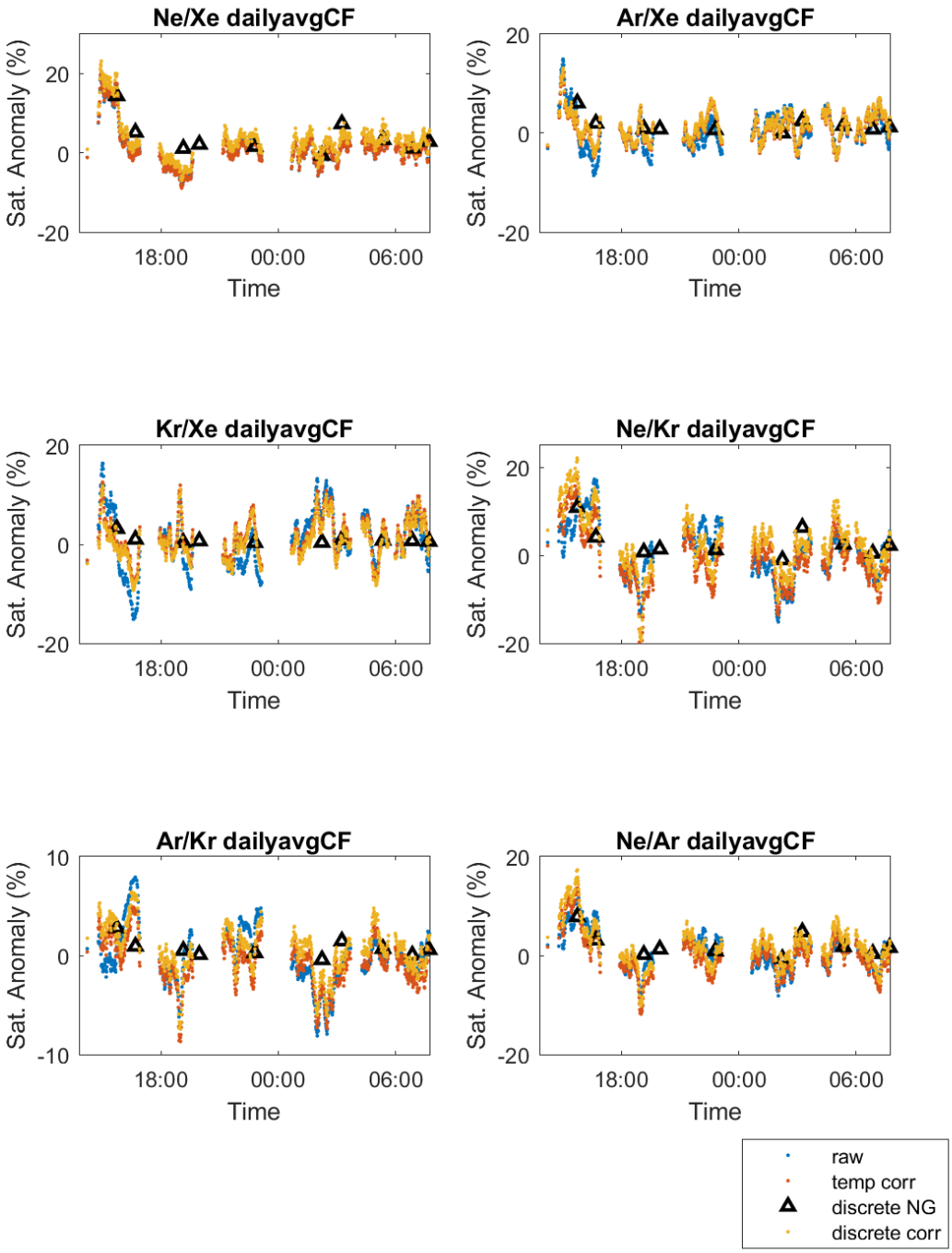

Figure 21. Temperature corrected GEMS continuous noble gas ratio was corrected by daily average correction factor for Day 1 (experiments 1 - 6). The plot also includes raw GEMS saturation anomaly data (blue), temperature corrected data (orange), and discrete noble gas results (black triangles).

The option of using daily average correction factor was considered because we observed a significant flattening of GEMS signal size for noble gas ratios such as Ar/Xe, Kr/Xe, and Ar/Kr with the linear regression correction factor. Based on an optimization calculation comparing the corrected GEMS data with the discrete noble gas data, however, we decided that the linear regression cost function was better. The root mean square error (rmse) was calculated from the difference between the discrete noble gas saturation anomaly ratio and the corresponding GEMS ratio using the two correction methods (Figure 22). For the linear regression correction, the rmse was 0.016 and for the daily average correction it was 0.023 for Ne/Xe. The linear regression slope was selected to be the better correction method because it has a smaller rmse. In doing the optimization calculation, we focused on the results from Ne/Xe. This was because Ne and Xe have the biggest differences in chemical characteristics of solubility and diffusivity. Therefore, we expected it to be most sensitive to the effects based on bubbles and diffusive gas exchange. Additionally, Ne/Xe data often showed variations larger than the noise when comparing the saturation anomalies of the discrete noble gas ratios to the GEMS noise (Figure 23). The GEMS noise was calculated as the precision of night-time air only values (Table 8). Since Ne/Xe is likely to have our best signal-to-noise ratio and is a good choice to study closely, the rest of this thesis focuses on the Ne/Xe GEMS data and the discrete noble gas data.

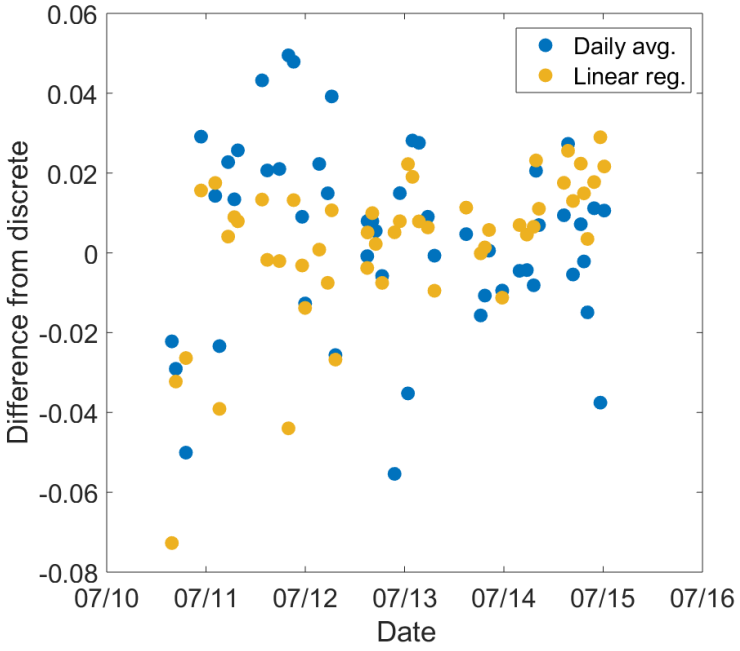

Figure 22. The difference between GEMS corrected saturation anomaly ratio and discrete noble gas saturation anomaly ratio using either daily average correction factor (blue) or linear regression correction factor (yellow). The root mean square error for the linear regression correction method was 0.016 and for the daily average correction method was 0.023.

	Ne/Xe	Ar/Xe	Kr/Xe	Ne/Kr	Ar/Kr	Ne/Ar
Day 1	1.5	1.1	1.2	1.1	0.6	1.1
Day 2	0.9	2.2	2.9	2.7	0.9	1.9
Day 3	1.0	1.6	2.4	2.2	1.0	1.3
Day 4	0.9	2.2	3.3	2.5	1.0	1.6
Day 5	0.8	1.0	1.1	1.1	0.3	0.9

Table 8. GEMS precisions for Ne/Xe, Ar/Xe, Kr/Xe, Ne/Kr, Ar/Kr, and Ne/Ar on each day. The daily precision of GEMS (%) was calculated using the overnight data for each day and for each ratio.

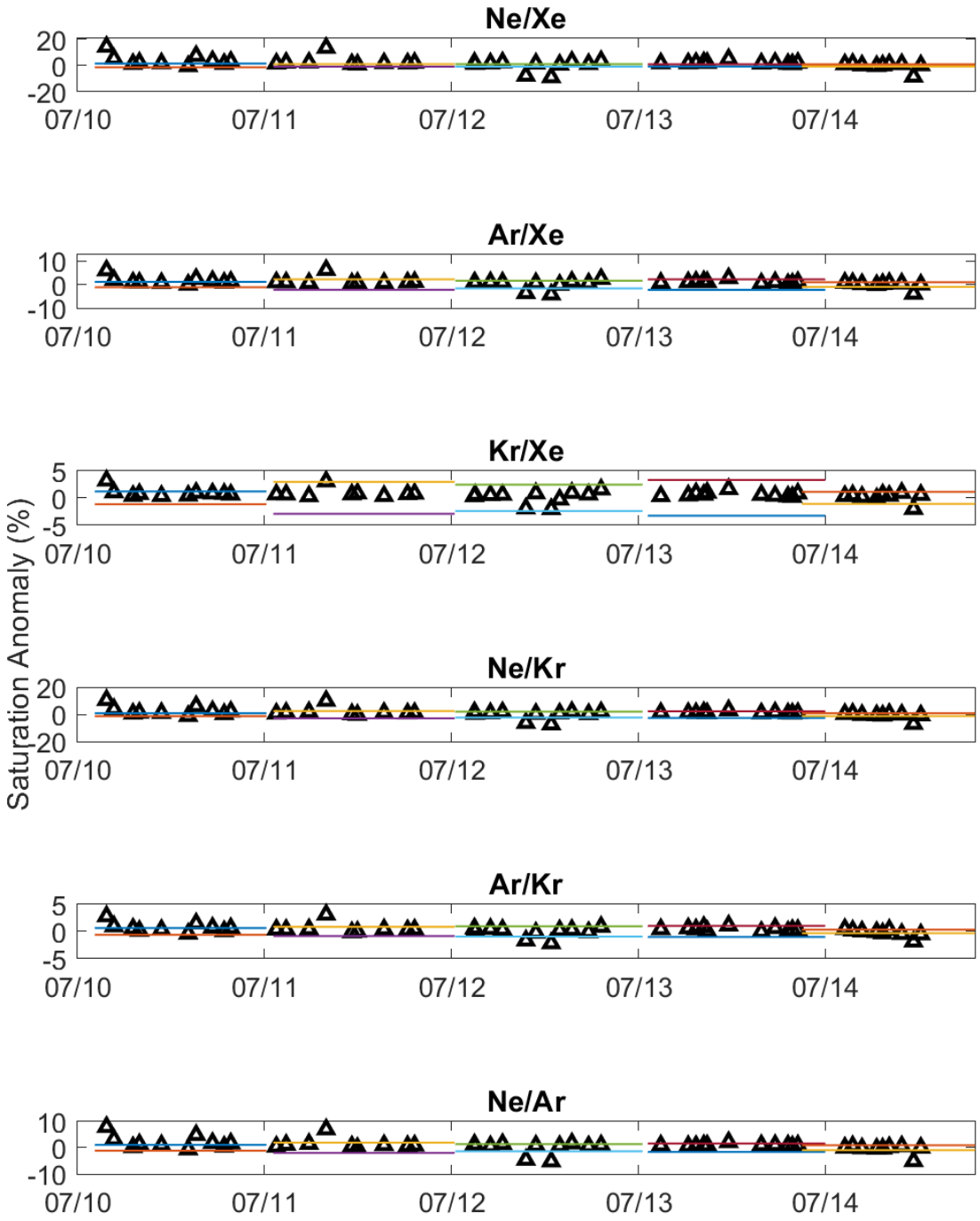

Figure 23. GEMS precision value for each day was calculated using the overnight data and was compared against the discrete noble gas saturation anomaly. Different combinations of color bars represent the upper and lower limit of the daily GEMS precision for a given ratio calculated form the overnight data. More of the Ne/Xe discrete noble gas ratios are outside of the GEMS margin of error.

Chapter 4. Results and Discussion

4.1. GEMS continuous Ne/Xe

To observe the behavior of noble gases throughout the experiment, GEMS continuous Ne/Xe saturation anomaly was plotted as a function of the experimental duration. The plots were created based on four conditions in the order of experimental conditions: uniform waves at 26°C, 20°C, and 32°C as well as JONSWAP waves at 26°C (Figures 24 - 27).

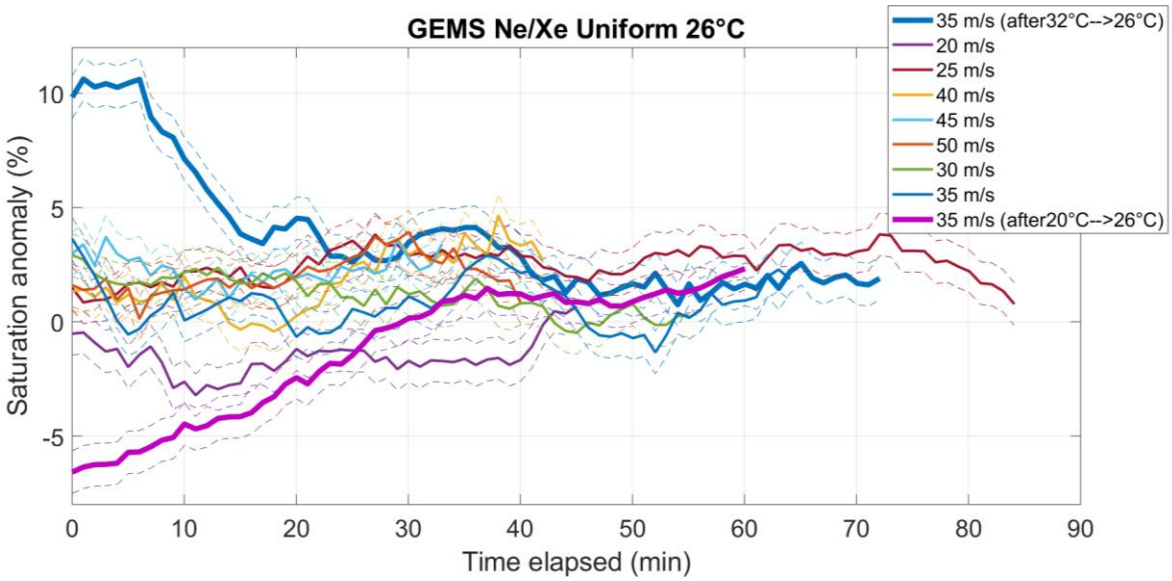

Figure 24. Ne/Xe saturation anomalies obtained from GEMS continuous data were plotted as a function of experiment duration for experiments with uniform waves at 26°C water temperature. Different colored lines represent different experiments with the wind speeds as indicated in the legend. Dashed lines surrounding the solid lines represent the upper and lower limits of GEMS saturation anomaly errors.

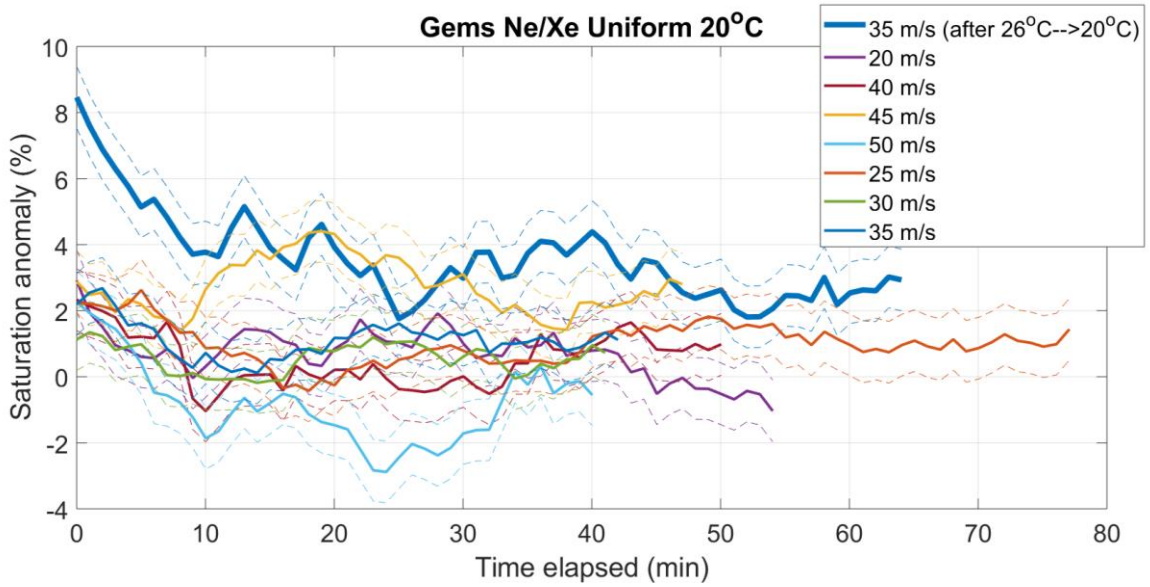

Figure 25. Ne/Xe saturation anomalies obtained from GEMS continuous data were plotted as a function of experiment duration for experiments with uniform waves at 20°C water temperature. Different colored lines represent different experiments with wind speeds as indicated in the legend. Dashed lines surrounding the solid lines represent the upper and lower limits of GEMS saturation anomaly errors.

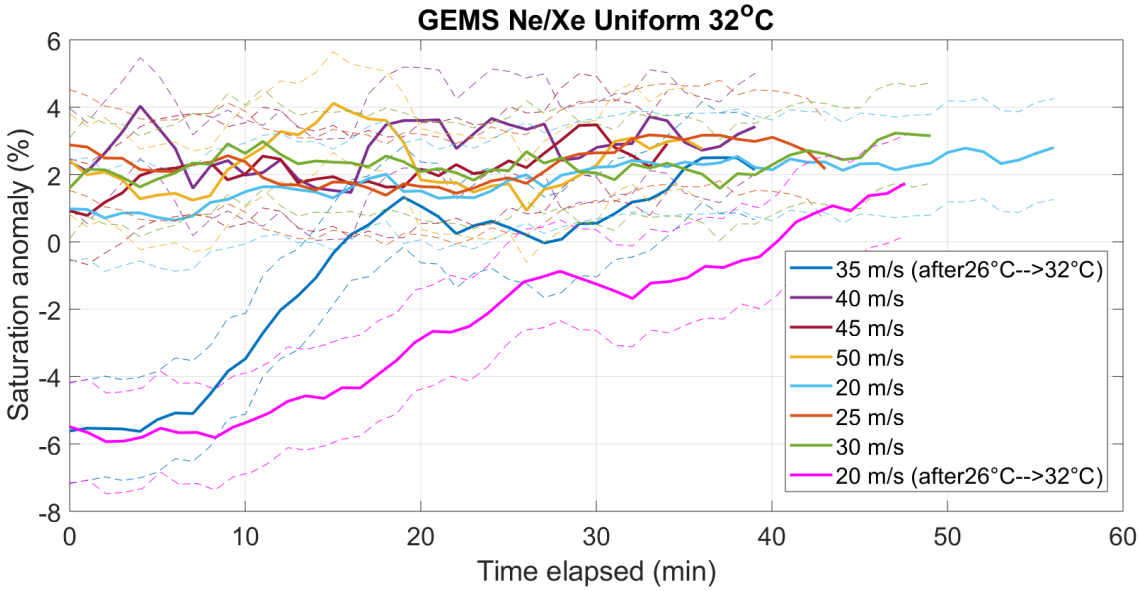

Figure 26. Ne/Xe saturation anomalies obtained from GEMS continuous data were plotted as a function of experiment duration for experiments with uniform waves at 32°C water temperature. Different colored lines represent different experiments with wind speeds as indicated in the legend. Dashed lines surrounding the solid lines represent the upper and lower limits of GEMS saturation anomaly errors.

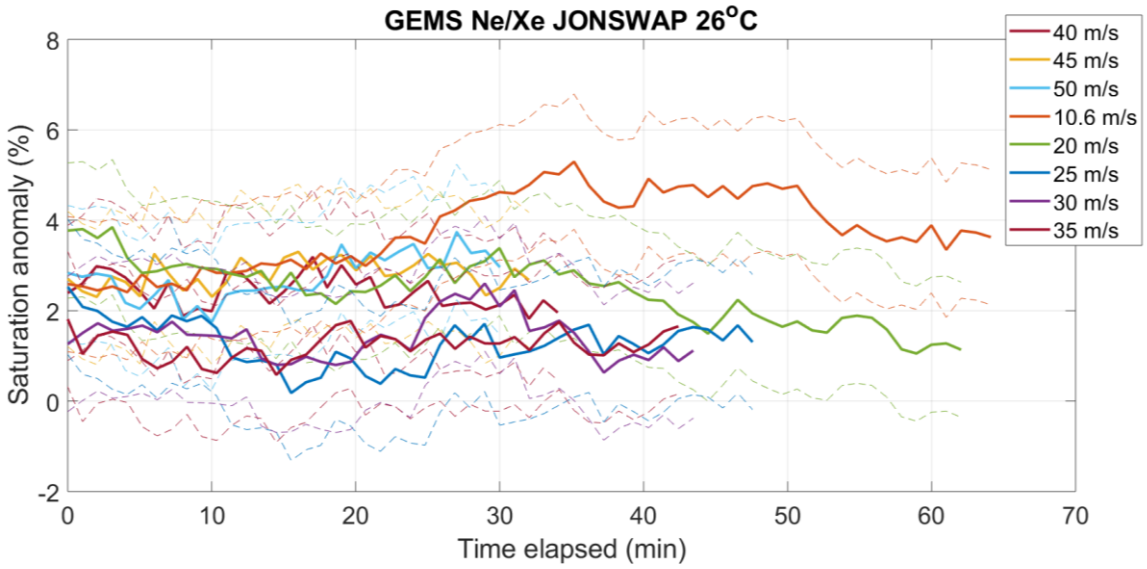

Figure 27. Ne/Xe saturation anomalies obtained from GEMS continuous data were plotted as a function of experiment duration for experiments with JONSWAP waves at 26°C water temperature. Different colored lines represent different experiments with wind speeds as indicated in the legend. Dashed lines surrounding the solid lines represent the upper and lower limits of GEMS saturation anomaly errors. Note: Experiments 25 and 26 are omitted from this figure due to their different wave settings.

4.1.1. Variations of Ne/Xe saturation anomaly within each experiment

From the saturation anomaly result for experiments involving prior heating and cooling, we can conclude that GEMS was able to successfully track the supersaturation and undersaturation of the noble gases. The tank water was cooled down from 32°C to 26°C in Experiment 1 and was warmed from 20°C to 26°C in Experiment 17 prior to the experiment (both experiments took place at condition of uniform waves with 35 m s^{-1} wind speed). When the tank water is cooled with little changes in gas concentration, as in the case of Experiment 1, the saturation anomaly of Ne/Xe becomes positive due to the fact that Xe undergoes a greater increase in solubility than Ne and becomes highly undersaturated. The opposite effect occurs in Experiment 17 when the tank water is warmed prior to the experiment. As the winds and waves promote diffusive and bubble mediated gas exchange, we expect the saturation anomaly to become increasingly closer to zero as the experiment progresses, which is in fact what we observe in our result.

Separate from the large changes in saturation anomalies over the course of

experimental duration for experiments involving prior heating/cooling, we observed variations of Ne/Xe saturation anomaly on time scales of approximately 10 to 20 minutes – "humps and dips" – in many of the experiments. For example, in Experiment 4, with 40 m s^{-1} wind speed and uniform waves at 26°C water temperature, Ne/Xe saturation anomaly climbed from ~0% to ~5% between about 15 - 40 minutes (Figure 24). It is unclear as to whether the saturation anomaly would have decreased again had we extended the experimental duration. However, if the water has reached a steady state equilibrium, we expect the saturation anomaly to eventually flatten and reach a steady value. Similarly, at 20°C water temperature, the saturation anomaly of Experiment 12 at wind speed 45 m s^{-1} gradually increased about ~3% and relaxed back to its original levels in between the period of 10 - 40 minutes since the start of the experiment (Figure 25). The observed increase in saturation anomaly is greater than the GEMS noise range. Therefore, we believe that the observed variation in Ne/Xe is reflective of actual changes in the physical condition. Another prominent increase in Ne/Xe saturation anomaly was seen in Experiment 8 with uniform waves at 26°C water temperature and wind speed 35 m s^{-1} (Figure 24). In some cases, we saw decreases in the Ne/Xe saturation anomalies during the course of the experiment, for example, in Experiment 13 at wind speed 50 m s^{-1} for uniform waves with 20°C water temperature, the saturation anomalies decreased between 15 - 25 minutes (Figure 25).

One of the possible physical changes behind the observed variations in Ne/Xe saturation anomaly is change in water temperature. This possibility was ruled out, however, as the water temperature was fairly constant; even when it was changing, the pattern did not trace that of the GEMS Ne/Xe ratio (Figures 28 - 31). For example, for Experiment 4, the water temperature remained essentially constant throughout the duration of the experiment (Figure 28). Similarly, for Experiment 12, the water temperature remained consistently between 20°C and 20.5°C, over the period of 10 - 40 minutes when the large "hump" was observed in the corresponding GEMS saturation anomaly ratio (Figure 29).

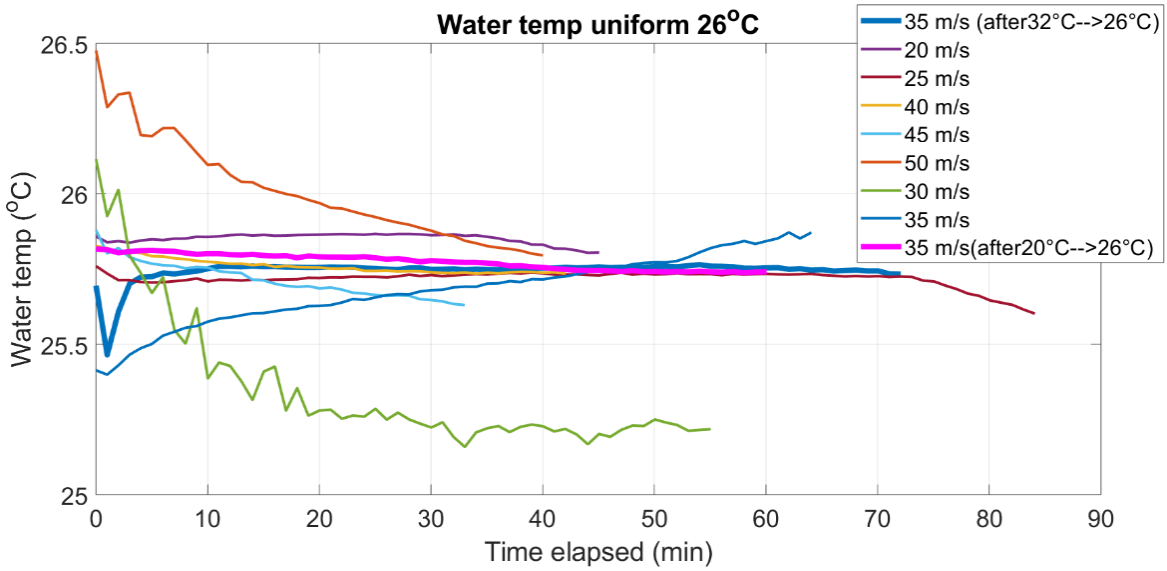

Figure 28. Change in water temperature over the course of experiments at uniform wave with water temperature at 26°C. Little change in water temperature is seen for Experiment 4 (wind speed 40 m s^{-1}) where a "hump" in saturation anomaly was observed in the GEMS data in between 15 - 40 minutes.

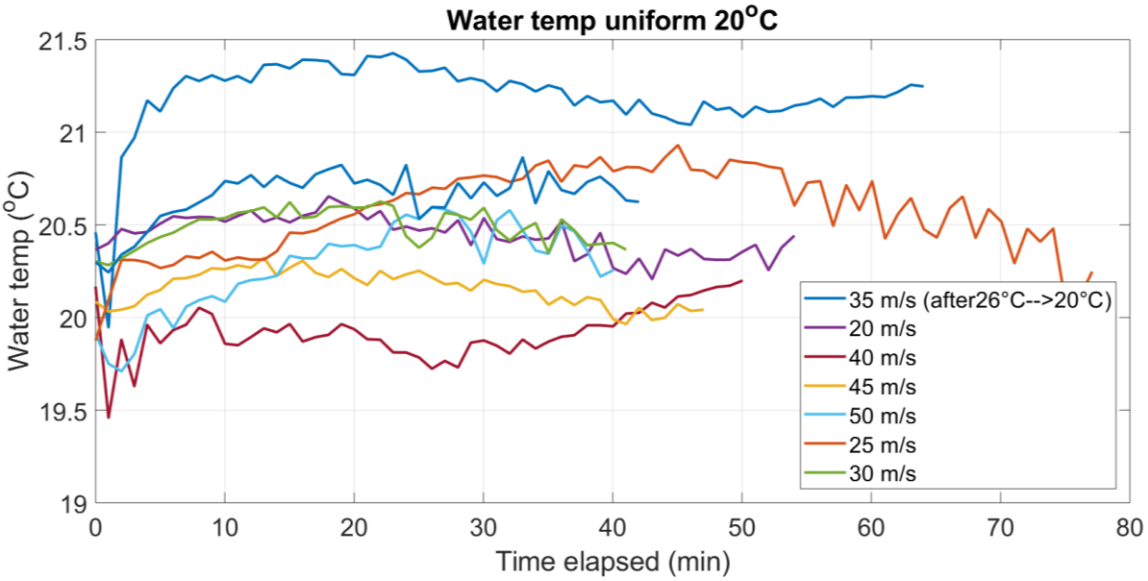

Figure 29. Change in water temperature over the course of experiments at uniform wave with water temperature at 20°C. Little change in water temperature is seen for Experiment 12 (wind speed 45 m s^{-1}) where a "hump" in saturation anomaly was observed in the GEMS data in between 10 - 40 minutes.

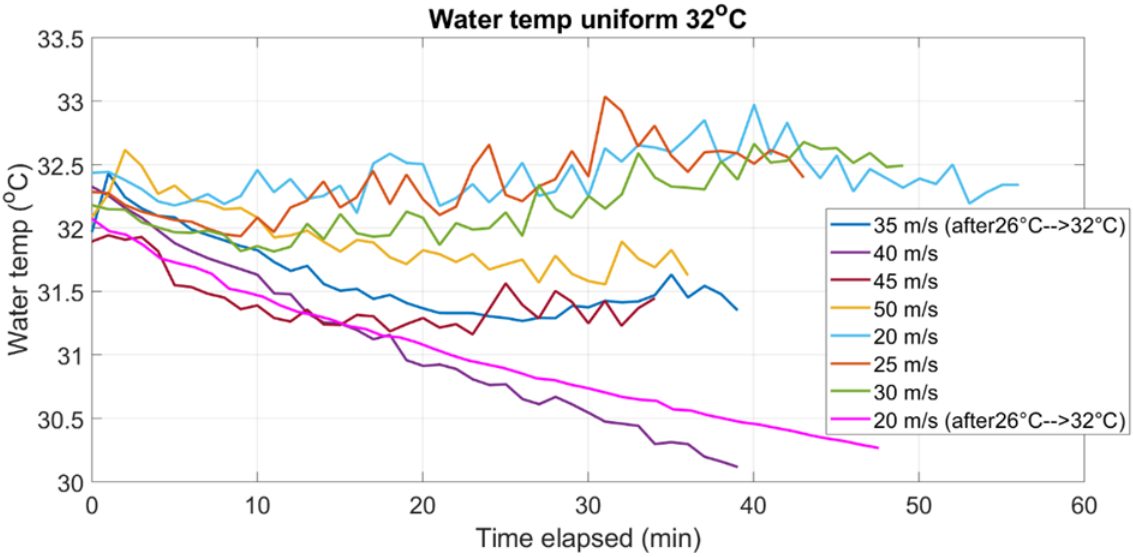

Figure 30. Change in water temperature over the course of experiments at uniform wave with water temperature at 32°C. The water temperature became gradually lower throughout the course of the experiment in Experiments 19 (wind speed 40 m s^{-1}) and 22 (wind speed 20 m s^{-1}) but GEMS results do not follow the pattern in respective experiments. For Experiment 21 (wind speed 50 m s^{-1}), in which we observe a "hump" between about 10 - 20 minutes into the experiment, we do not see a drastic change in water temperature.

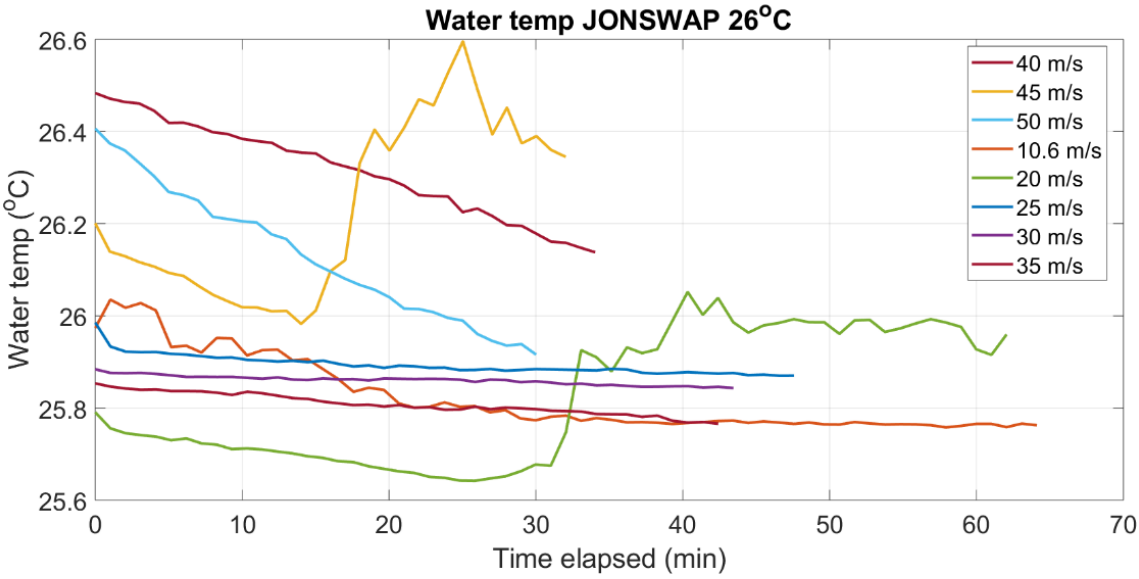

Figure 31. Change in water temperature over the course of experiments at JONSWAP waves with water temperature at 26°C. The water temperature remained fairly constant for all experiments. Note: Experiments 25 and 26 are omitted from this figure due to their different wave settings.

To explore whether the local variations in Ne/Xe are related to the increase or decrease of bubbles, GEMS Ne/Xe data for Experiments 4 and 5 were plotted at the same time as the integrated bubble volume for the duration of the experiments (Figure 32). The result shows that the local changes in GEMS Ne/Xe saturation anomaly closely follow the change in pattern of the total volume of bubbles—it is interesting to see that there is up to about 5 minutes of delay in which the noble gas result to follow the increase or decreasing pattern of bubble volume. Moreover, the variations in the GEMS data were observed in experiments with wind speeds greater than or equal to 35 m s^{-1}. This supports the idea that the local increases and decreases are related to bubbles, since bubble fluxes are expected to become more significant at higher wind speeds. The possible changes in the bubble volume may be caused by variation in the wave paddle function or variation in wind speeds. Unfortunately, we cannot examine the correlation between the bubble variation and wind speeds since we do not have continuous wind speed data after the first minute of the experiments. Thus, further testing is necessary to confirm the reason behind the bubble volume variation.

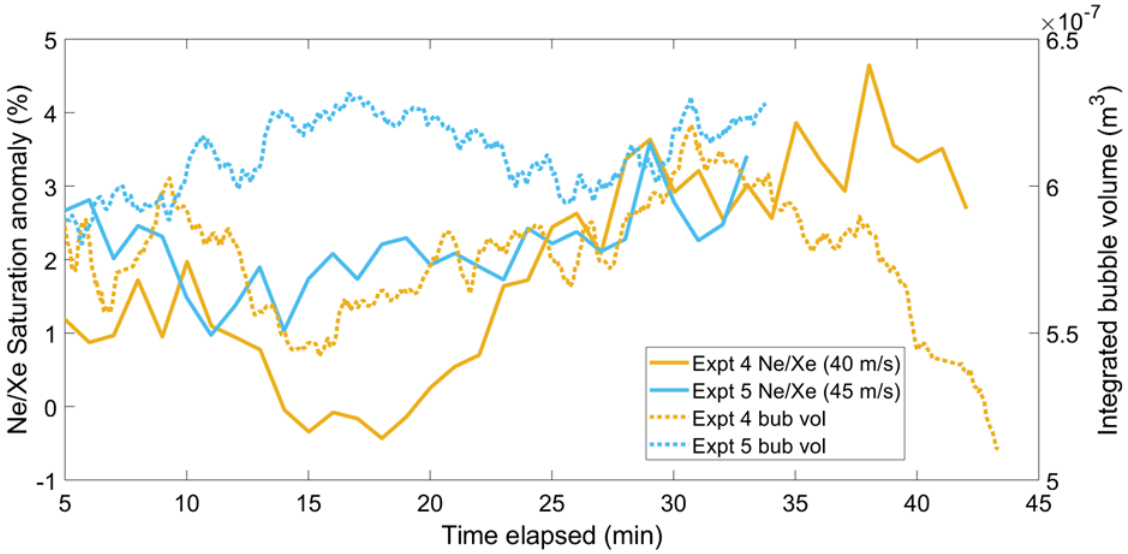

Figure 32. Integrated bubble volume and Ne/Xe saturation anomaly are plotted together for Experiments 4 and 5 over the experimental duration. The integrated bubble volume reflects the volume of bubbles captured by the bubble imager. The increase and decrease in integrated bubble volume result correspond to the increase and decrease in the GEMS saturation anomaly. *Bubble volume data credit: Andrew Wyatt Smith, University of Miami SUSTAIN Laboratory, by personal communication.*

4.1.2. Initial vs. final saturation anomalies

Whether the equilibrium saturation anomalies of gases depends on the initial saturation anomalies has been a topic of great interest to the scientific community studying air-sea gas exchange. From the GEMS result, we found that initial saturation states of the gases probably have little effect on saturation anomalies at the end of the expeirment, when the gases have presumably reached steady state. This was observed when comparing two experiments involving temperature change in which the differences in initial saturation anomalies (Table 9) were greater than the Ne/Xe GEMS noise range (Table 8). One set of experiments we examined was Experiments 1 and 17, with uniform waves at 26°C and wind speed 35 m s^{-1} condition involving prior cooling (Experiment 1) and prior warming (Experiment 17) (Figure 24). In Experiment 1, GEMS Ne/Xe is 9.8% saturated at the start whereas in Experiment 17, it is 6.6% undersaturated. The final saturation anomaly for Experiment 1 was 1.9% and for Experiment 17 it was 2.3%. The range of differences in the final saturation anomaly was 0.0 - 0.4%, which is within the GEMS noise range. Thus, we

can conclude that regardless of the differences in initial saturation anomalies, the final saturation anomalies were about the same. The other set of experiments we looked at was uniform waves at 20°C with wind speed 35 m s^{-1} involving prior cooling (Experiment 9) and no temperature change (Experiment 16) (Figure 25). While the initial saturation anomalies were much different, the final Ne/Xe saturation anomalies were 3.0% (Experiment 9) and 1.1% (Experiment 16). The difference in the final saturation anomalies (1.9%) is within the upper and lower limits of GEMS noise for Day 2 and Day 3 when the experiments were conducted, which was 1.8% (0.9% × 2) and 2.0% (1.0% × 2), respectively (see Table 8 for GEMS precision). Since the GEMS values at the end of the experiment seem to be still changing for Experiment 9, one might even argue that had the experiment was given more time to reach steady state, the difference in the final values between the experiments would have been smaller.

	Uniform 20°C		Uniform 26°C		
Prior condition	26°C→20°C	20°C	32°C→26°C	20°C→26°C	26°C
Experiment #	9	16	1	17	8
Wind speed (m/s)	35	35	35	35	35
Initial (%)	8.5	2.3	9.8	-6.6	3.6
Final (%)	3.0	1.1	1.9	2.3	1.9
| Diff. between final (%) |	1.9		0.0 - 0.4		

Table 9. Comparison of GEMS initial and final saturation anomalies for sets of experiments involving temperature change. The initial differences in saturation anomalies make little effect on the steady-state saturation anomalies when comparing experiments involving prior temperature change. The GEMS noise range was +/- 0.8% - 1.5% depending on the experiment day.

It is notable that the initial noble gas saturation anomalies were clustered around 2% for all of the experiments that did not start right after cooling/heating of the tank. One explanation behind the observed initial supersaturation is that the equilibration effort between experiments may not have produced the effect that we had hoped for. We had intended to

"reset" the gases by exposing the tank water to gentle winds and waves for about an hour in between experiments to promote equilibration. However, it could have been that the equilibration did not fully equilibrate the gases from the previous experimental condition and perhaps even that the equilibration condition itself could have been acting to create supersaturation. The other possibility is that the GEMS continuous result is overestimating the saturation anomaly, whether due to the employed correction method or due to instrumental limitation.

For the majority of experiments, the difference between final Ne/Xe saturation anomalies between experiments were about 2 - 3 % at most for a given condition. The fact that most of the experiments ended in slight supersaturation of Ne/Xe was expected as it shows the effect of bubble-mediated gas exchange. The variation of the final Ne/Xe saturation anomalies is within the GEMS noise range (between $0.8 \times 2 = 1.6\%$ and $1.5 \times 2 = 3.0\%$, see Table 8). Some of the differences in the final values may also be affected by whether the experiment has reached steady state equilibrium or not. For some experiments, such as Experiments 12 and 13 (uniform waves at 20°C with 45 m s^{-1} and 50 m s^{-1} wind speeds, respectively) as well as Experiment 35 (uniform waves at 32°C with 20 m s^{-1}) the Ne/Xe saturation anomalies had not leveled off by the time the experiment ended. This suggests that the gases in these experiments have not achieved the steady state equilibrium at the time when the winds and waves were stopped.

In conclusion, the comparison of experiments involving prior warming/cooling of the tank water suggest that initial state does not affect the steady state saturation anomalies. However, for the majority of the other experiments, looking at the GEMS continuous result itself cannot provide us with concrete evidence since the differences in the initial and final saturation anomalies fall between the GEMS noise range (1.6% - 3.0%). Therefore, the initial and final discrete saturation anomalies will be further explored in the subsequent section using the discrete noble gas results.

4.2. Initial vs. final discrete noble gas

4.2.1. Ne/Xe Saturation anomalies

The concentrations for discrete noble gas samples for He, Ne, Ar, Kr, and Xe at the beginning ("initial") of select experiments and at the end ("end") of all the experiments were obtained (Table 10). From the discrete noble gas concentrations, saturation anomalies for Ne/Xe were calculated. Table 11 shows the initial and final discrete saturation anomalies for experiments that did not involve prior warming/cooling of the tank while Table 12 shows the results for the experiments directly following change in the tank water temperature. Figure 33 summarizes all the discrete noble gas results.

Expt. #	Expt. Day	Sample #	Dupli-cate	C(He) mol/kg	C(Ne) mol/kg	C(Ar) mol/kg	C(Kr) mol/kg	C(Xe) mol/kg
1	One	1	0	1.848E-09	7.140E-09	1.004E-05	2.104E-09	2.704E-10
1	One	2	0	1.825E-09	7.174E-09	1.055E-05	2.250E-09	2.954E-10
2	One	1	0	1.740E-09	6.867E-09	1.038E-05	2.222E-09	2.934E-10
2	One	2	0	1.756E-09	6.899E-09	1.034E-05	2.224E-09	2.929E-10
3	One	1	0	1.755E-09	6.904E-09	1.037E-05	2.227E-09	2.943E-10
4	One	1	0	1.714E-09	6.758E-09	1.029E-05	2.222E-09	2.932E-10
4	One	2	0	1.882E-09	7.366E-09	1.066E-05	2.262E-09	2.972E-10
5	One	1	0	1.787E-09	7.039E-09	1.050E-05	2.244E-09	2.955E-10
5	One	1	1	1.787E-09	7.040E-09	1.049E-05	2.245E-09	2.952E-10
6	One	2	0	1.732E-09	6.810E-09	1.017E-05	2.178E-09	2.853E-10
6	One	3	0	1.783E-09	7.023E-09	1.047E-05	2.239E-09	2.951E-10
7	Two	1	0	1.740E-09	6.861E-09	1.031E-05	2.206E-09	2.893E-10
7	Two	1	1	1.736E-09	6.848E-09	1.030E-05	2.209E-09	2.913E-10
7	Two	2	0	1.754E-09	6.935E-09	1.045E-05	2.248E-09	2.970E-10
8	Two	1	0	1.780E-09	7.008E-09	1.046E-05	2.236E-09	2.956E-10
8	Two	1	1	1.770E-09	6.974E-09	1.042E-05	2.239E-09	2.958E-10
9	Two	1	0	1.744E-09	6.897E-09	1.040E-05	2.226E-09	2.943E-10
9	Two	2	0	1.773E-09	7.116E-09	1.124E-05	2.459E-09	3.316E-10
10	Two	1	0	1.731E-09	6.996E-09	1.121E-05	2.477E-09	3.351E-10

10	Two	2	0	1.739E-09	7.031E-09	1.135E-05	2.505E-09	3.384E-10
11	Two	1	0	1.787E-09	7.198E-09	1.151E-05	2.532E-09	3.439E-10
12	Two	1	0	1.794E-09	7.234E-09	1.158E-05	2.547E-09	3.445E-10
13	Two	1	0	1.761E-09	7.119E-09	1.145E-05	2.525E-09	3.422E-10
13	Two	2	0	1.786E-09	7.173E-09	1.147E-05	2.521E-09	3.406E-10
14	Three	1	0	1.778E-09	7.160E-09	1.144E-05	2.514E-09	3.419E-10
14	Three	2	0	1.763E-09	7.102E-09	1.144E-05	2.525E-09	3.425E-10
15	Three	1	0	1.756E-09	7.061E-09	1.144E-05	2.531E-09	3.431E-10
15	Three	2	0	1.769E-09	7.135E-09	1.146E-05	2.519E-09	3.415E-10
16	Three	1	0	1.790E-09	7.210E-09	1.143E-05	2.514E-09	3.399E-10
16	Three	1	1	1.792E-09	7.201E-09	1.144E-05	2.512E-09	3.402E-10
17	Three	1	0	1.729E-09	6.910E-09	1.096E-05	2.398E-09	3.242E-10
17	Three	2	0	1.756E-09	6.907E-09	1.039E-05	2.242E-09	2.948E-10
18	Three	1	0	1.740E-09	6.806E-09	1.022E-05	2.196E-09	2.890E-10
18	Three	2	0	1.748E-09	6.703E-09	9.436E-06	1.976E-09	2.547E-10
19	Three	1	0	1.762E-09	6.793E-09	9.664E-06	2.037E-09	2.620E-10
20	Three	1	0	1.746E-09	6.706E-09	9.471E-06	1.992E-09	2.547E-10
21	Three	1	0	1.745E-09	6.693E-09	9.406E-06	1.958E-09	2.479E-10
22	Four	1	0	1.727E-09	6.608E-09	9.271E-06	1.936E-09	2.480E-10
23	Four	1	0	1.716E-09	6.567E-09	9.213E-06	1.920E-09	2.453E-10
24	Four	1	0	1.706E-09	6.527E-09	9.197E-06	1.923E-09	2.453E-10
24	Four	2	0	1.726E-09	6.608E-09	9.243E-06	1.921E-09	2.451E-10
25	Four	1	0	1.710E-09	6.561E-09	9.266E-06	1.946E-09	2.485E-10
25	Four	2	0	1.751E-09	6.868E-09	1.013E-05	2.151E-09	2.798E-10
26	Four	1	0	1.760E-09	6.879E-09	1.023E-05	2.197E-09	2.886E-10
27	Four	1	0	1.749E-09	6.875E-09	1.027E-05	2.192E-09	2.889E-10
28	Four	1	0	1.749E-09	6.873E-09	1.025E-05	2.201E-09	2.902E-10
29	Four	1	0	1.735E-09	6.826E-09	1.021E-05	2.185E-09	2.881E-10
29	Four	2	0	1.753E-09	6.909E-09	1.035E-05	2.220E-09	2.918E-10
30	Five	1	1	1.717E-09	6.764E-09	1.019E-05	2.179E-09	2.873E-10
30	Five	2	0	1.716E-09	6.757E-09	1.017E-05	2.186E-09	2.884E-10
31	Five	1	0	1.708E-09	6.723E-09	1.018E-05	2.188E-09	2.891E-10

32	Five	1	0	1.707E-09	6.711E-09	1.018E-05	2.191E-09	2.906E-10
33	Five	1	0	1.704E-09	6.712E-09	1.018E-05	2.197E-09	2.892E-10
33	Five	2	0	1.722E-09	6.786E-09	1.024E-05	2.195E-09	2.897E-10
34	Five	1	0	1.728E-09	6.806E-09	1.025E-05	2.215E-09	2.909E-10
35	Five	1	0	1.706E-09	6.674E-09	9.967E-06	2.133E-09	2.800E-10
35	Five	1	1	1.705E-09	6.667E-09	9.956E-06	2.128E-09	2.794E-10
35	Five	2	0	1.701E-09	6.568E-09	9.481E-06	2.014E-09	2.599E-10

Table 10. Discrete noble gas concentrations (mol/kg) for He, Ne, Ar, Kr, and Xe processed by the in-lab mass spectrometer at WHOI's Isotope Geochemistry Facility. Sample # indicates whether the sample was the first or second sample taken for the corresponding experiment. The duplicate sample points were later averaged, resulting in 53 total discrete noble gas samples. The precision obtained from duplicate sample for each gas was about 0.1 - 0.2% (uncertainty due to small sample size).

Wind speed (m/s)	10.6	20	25	30	35	40	45	50
Uniform 20°C								
Expt. #	-	10	14	15	16	11	12	13
Initial (%)	-	1.03	-	0.12	-	-	-	1.57
Final (%)	-	0.71	2.11* 1.21**	1.55	2.34	1.74	2.68	2.01
Final - Initial (%)	-	-0.32	-	1.42	-	-	-	0.44
Uniform 26°C								
Expt. #	-	2	3	7	8	4	5	6
Initial (%)	-	1.13	-	1.45	-	-0.60	-	1.22
Final (%)	-	2.17	1.62	2.09	2.21	7.35	3.37	2.89
Final - Initial (%)	-	1.04	-	0.64	-	7.95	-	1.68
Uniform 32°C								
Expt. #	-	22	23	24	-	19	20	21
Initial (%)	-	-	-	1.99	-	-	-	-
Final (%)	-	1.66	1.70	2.40	-	2.91	1.06	3.39
Final - Initial (%)	-	-	-	0.41	-	-	-	-
JONSWAP 26°C								
Expt. #	30	31	32	33	34	27	28	29
Initial (%)	0.84	-	-	-0.02	-	-	-	0.97
Final (%)	1.23	0.00	-0.52	0.96	1.02	2.06	1.14	2.00
Final - Initial (%)	0.38	-	-	0.97	-	-	-	1.03

Table 11. Initial and final discrete saturation anomalies for Ne/Xe was calculated for experiments that did not directly follow cooling/warming of the tank. For experiments above wind speed 40 m s^{-1} the initial and final samples were both taken outside of the experimental period (ex. initial was taken right before the winds and waves have started) with the exception of Expt. 4 with uniform waves at 26°C with 40 m s^{-1} wind speed. The average initial values across different experiments was 0.88% +/- 0.76 (n=11). *Copper tube sample was collected 0 minutes after the experiment end time. ** Copper tube sample was collected 5 minutes after the experiment end time.

	Uniform 20°C	Uniform 26°C		Uniform 32°C
Prior condition	26°C→20°C	32°C→26°C	20°C→26°C	26°C→32°C
Experiment #	9	1	17	18
Wind speed (m/s)	35	35	35	35
Initial (%)	13.60	14.41	-7.91	-9.09
Final (%)	2.00	5.19	1.44	0.57
Final - Initial (%)	-11.60	-9.21	9.34	9.66

Table 12. Initial and final Ne/Xe discrete sample saturation anomalies for experiments taken right after the warming/cooling of the tank.

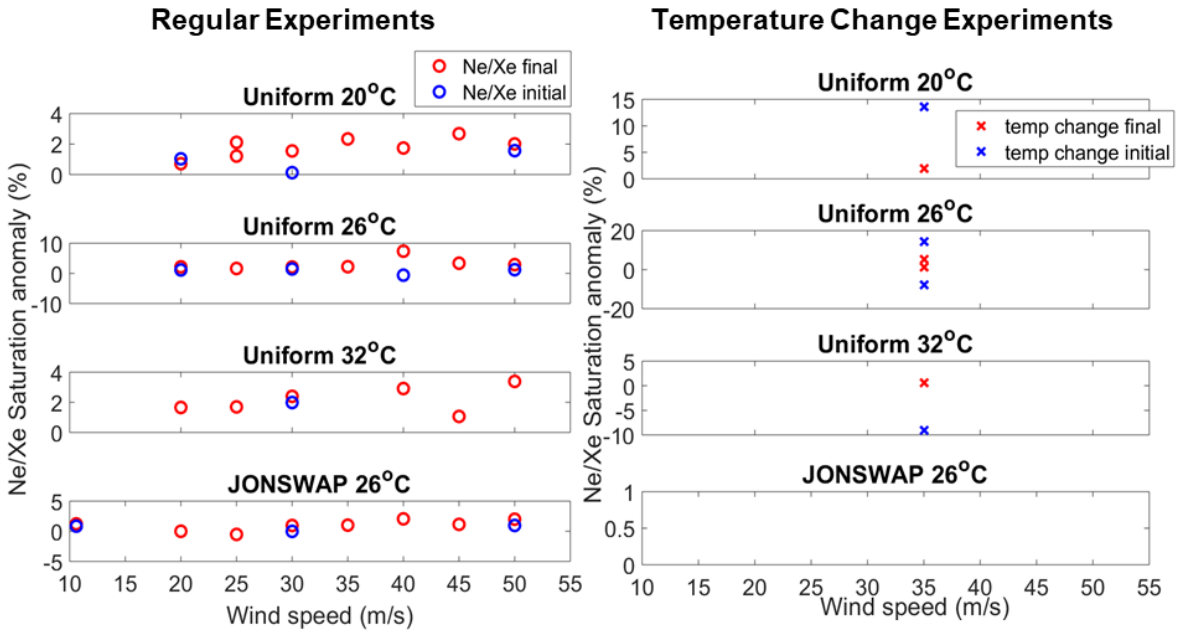

Figure 33. Initial and final Ne/Xe saturation anomalies calculated from the discrete samples. The crosses represent saturation anomalies from experiments conducted right after warming/cooling of the tank water and the circles represent saturation anomalies from the rest of the experiments. Initial saturation anomaly is denoted in blue and the final in red. Final discrete samples for experiments with wind speeds 40 m s^{-1} or above were taken right after the experiment, once the waves and winds were stopped (except for the sample taken at uniform waves at 26°C).

For many of the experiments with higher wind speeds, the discrete noble gas samples were taken outside of the experimental duration. For example, the initial sample was taken right before, and the final sample was taken immediately after the winds and waves

were turned on. We used different sampling methods for higher wind speed experiments to prevent bubbles from directly entering our copper tube, as we are interested in the concentration of gases that were truly dissolved in the water of the wind-wave tank. Undissolved, entrained bubbles due to wave breaking in the sample will overestimate the actual saturation anomaly of the gases in the water. The differences in the two final Ne/Xe saturation anomaly values from Experiment 14 indicate that saturation anomaly is substantially different whether taking the sample right before or after the winds and waves have stopped. For Experiment 14, the higher saturation anomaly value (2.11%) is from a sample taken 0 minutes after the winds and waves were stopped whereas the lower saturation anomaly value (1.21%) is from a sample taken 5 minutes after the winds and waves have stopped (uncertainties in discrete values are 0.1 - 0.2%). Therefore, for the higher wind speed experiments, which we have taken the copper tube sample a few minutes after the experiment end time, the saturation anomalies may be slightly underestimated compared to samples taken during the experiments for lower wind speed conditions. A complete information on the timing of discrete noble gas sampling can be found in Table 1 in the Methods chapter.

To see whether the equilibrium saturation anomaly is affected by the initial saturation anomaly, two sets of experiments involving prior warming/cooling of the tank were compared, similar to what was done in the previous section for GEMS (Table 13).

	Uniform 20°C		Uniform 26°C		
Prior condition	26°C→20°C	20°C	32°C→26°C	20°C→26°C	26°C
Experiment #	9	16	1	17	8
Wind speed (m/s)	35	35	35	35	35
Initial (%)	13.60	-	14.41	-7.91	-
Final (%)	2.00	2.34	5.19	1.44	2.21
| Diff. between final (%) |	0.34		0.77 - 3.75		

Table 13. Comparison of initial and final Ne/Xe discrete sample saturation anomalies for sets of experiments involving prior warming/cooling of the tank.

The range of differences in the final saturation anomaly across different experiments at uniform waves with 26°C water temperature was 0.77 - 3.75%. However, it is difficult to tell whether the 3.75% difference is due to actual difference in the noble gas saturation anomaly or the sampling timing. The copper tube sample for Experimetnt 1 was taken 10 minutes *before* the experiment ended, and for Experiment 17 the sample was taken 5 minutes *after* the experiment ended. As sampling timing was shown to affect the noble gas saturation anomaly substantially, it is most likely that the differences in saturation anomalies would have been smaller than 3.75% had the copper tube sample for Experiment 1 been taken after the experiment. The difference between the final saturation anomalies for Experiments 9 and 16 was 0.34%. In this case, the final discrete noble gas sampling timing was very similar (4 and 3 minutes after experiment, respectively).

Discrete noble gas results can also inform us about the reliability of the initial supersaturation observed in the GEMS continuous noble gas data (Figures 24 - 27). From the average initial discrete noble gas saturation anomaly result and the result from Experiment 30, it is most probable that the initial supersaturation for GEMS continuous noble gas result around 2% is likely an overestimate. According to the discrete samples, the average initial saturation anomaly was 0.88% with standard deviation of 0.76% (n=11), with six out of eleven initial conditions having a saturation anomaly value between 1 - 2% (Table 11). This result indicates that some of the experiments started out with slightly saturated conditions, but not to the extent that we observe in the GEMS data. To explore the possibility of whether the equilibration condition was actually causing the supersaturation, it is useful to look at the result from Experiment 30. Experiment 30 was conducted at wind speed 10.6 m s^{-1} with JONSWAP waves with peak period 1 second and 0.15 m wave amplitude, the closest condition to the equilibration condition. Given that the final saturation anomaly for Experiment 30 was 1.23%, it may be that the equilibration condition was not perfect and that it was causing the initial supersaturation seen in the GEMS data. Finally, comparing the Δsaturation anomaly (final − initial saturation anomaly) across differenet wind speeds for a given condition, only JONSWAP waves showed a consistent pattern, in which Δsaturation anomaly increased as the wind speed increased (Table 11).

In conclusion, Ne/Xe discrete saturation anomaly results show that the initial condition does not affect the final saturation anomaly because experiments starting at very different initial values ended up with similar steady state saturation anomalies. It is important to know that initial saturation states do not affect the conclusions about steady-state saturation anomalies. In fact, comparison between the result from experimental condition similar to that during equilibriation shows that the initial saturation anomalies may be dependent upon how well the gases equilibrated after the previous experiments. Thus, while it would be important to know the Δsaturation anomaly to calculate the total flux, we would not expect to see a consistent pattern against increasing wind speed.

4.2.2. Individual noble gas (He, Ne, Ar, Kr, and Xe) saturation anomalies

The initial and final steady state saturation anomalies for He, Ne, Ar, Kr and Xe were calculated from the discrete noble gas samples (Figure 34). The initial and final steady state saturation anomalies for He and Ne (the least soluble gases) and Xe (the most soluble gas) are also presented in tabular form (Table 14). The saturation anomalies of those three gases generally increased during the experiments. However, there were several exceptions, primarily for experiments conducted at less turbulent conditions (JONSWAP waves, lower wind speed) for Xe, which is least affected by bubble mediated gas exchange. As expected, Δsaturation anomalies for He and Ne were greater than for Xe for most experiments and for a given gas, Δsaturation anomaly did not always increase as the wind speed increased. For example, the Δsaturation anomaly for He and Ne with uniform wave at 26°C increased with wind speed for 20, 30 and 40 m s^{-1} but then decreased for wind speed of 50 m s^{-1}. Similarly, while the Δsaturation anomaly increased between 10.6 and 30 m s^{-1} for JONSWAP waves for He, Ne, and Xe, the Δsaturation anomaly value was lower for 50 m s^{-1} than that for 30 m s^{-1} (Table 14). This is consistent with the hypothesis that the initial conditions depend mostly on the extent of equilibration whereas the final conditions reflect steady state values that depend on wind/wave conditions of the actual experiment. Therefore, the difference between initial and final is meaningful primarily because those differences suggest which experiments had large fluxes and thus are good candidates for quantitative analysis of flux

with time.

Wind speed (m/s)		10.6	20	25	30	35	40	45	50
Uniform 20°C									
Initial (%)	He	-	3.77	-	5.50	-	-	-	5.24
	Ne	-	3.92	-	5.06	-	-	-	5.24
	Xe	-	2.86	-	4.93	-	-	-	3.61
Final (%)	He	-	4.37	6.56* 5.66**	6.52	7.81	6.71	7.10	6.91
	Ne	-	4.52	6.21* 5.34**	6.36	7.52	6.41	6.82	6.38
	Xe	-	3.78	4.01* 4.08**	4.74	5.06	4.59	4.03	4.29
Final - Initial (%)	He	-	0.60	-	1.02	-	-	-	1.67
	Ne	-	0.60	-	1.30	-	-	-	1.15
	Xe	-	0.92	-	-0.19	-	-	-	0.67
Uniform 26°C									
Initial (%)	He	-	5.46	-	5.45	-	3.39	-	5.14
	Ne	-	5.31	-	5.32	-	3.18	-	4.95
	Xe	-	4.13	-	3.82	-	3.80	-	3.69
Final (%)	He	-	6.70	6.34	6.75	8.13	14.00	8.30	8.09
	Ne	-	5.99	5.75	6.51	7.72	12.82	7.88	7.68
	Xe	-	3.74	4.06	4.33	5.39	5.09	4.36	4.66
Final - Initial (%)	He	-	1.24	-	1.30	-	10.61	-	2.95
	Ne	-	0.69	-	1.19	-	9.64	-	2.73
	Xe	-	-0.39	-	0.51	-	1.29	-	0.97
Uniform 32°C									
Initial (%)	He	-	-	-	4.94	-	-	-	-
	Ne	-	-	-	3.97	-	-	-	-
	Xe	-	-	-	1.95	-	-	-	-
Final (%)	He	-	5.88	5.51	6.27	-	6.86	6.42	6.92
	Ne	-	5.03	4.78	5.60	-	5.99	5.86	6.28
	Xe	-	3.32	3.03	3.13	-	2.99	4.75	2.80
Final - Initial (%)	He	-	-	-	1.33	-	-	-	-
	Ne	-	-	-	1.63	-	-	-	-
	Xe	-	-	-	1.18	-	-	-	-
JONSWAP 26°C									
Initial (%)	He	4.27	-	-	4.07	-	-	-	5.71
	Ne	4.08	-	-	3.77	-	-	-	5.49
	Xe	3.21	-	-	3.79	-	-	-	4.47
Final (%)	He	4.20	4.09	4.05	5.32	5.79	6.14	6.59	6.55
	Ne	3.84	3.78	3.59	5.07	5.46	5.71	6.20	6.32
	Xe	2.59	3.78	4.13	4.07	4.40	3.57	5.00	4.24
Final - Initial (%)	He	-0.08	-	-	1.25	-	-	-	0.83
	Ne	-0.23	-	-	1.29	-	-	-	0.83
	Xe	-0.62	-	-	0.28	-	-	-	-0.24

Table 14. Discrete saturation anomalies for He, Ne, and Xe were calculated for experiments that do not directly follow a change in tank water temperature. *Copper tube sample was collected 0 minutes after the experiment end time. ** Copper tube sample

was collected 5 minutes after the experiment end time.

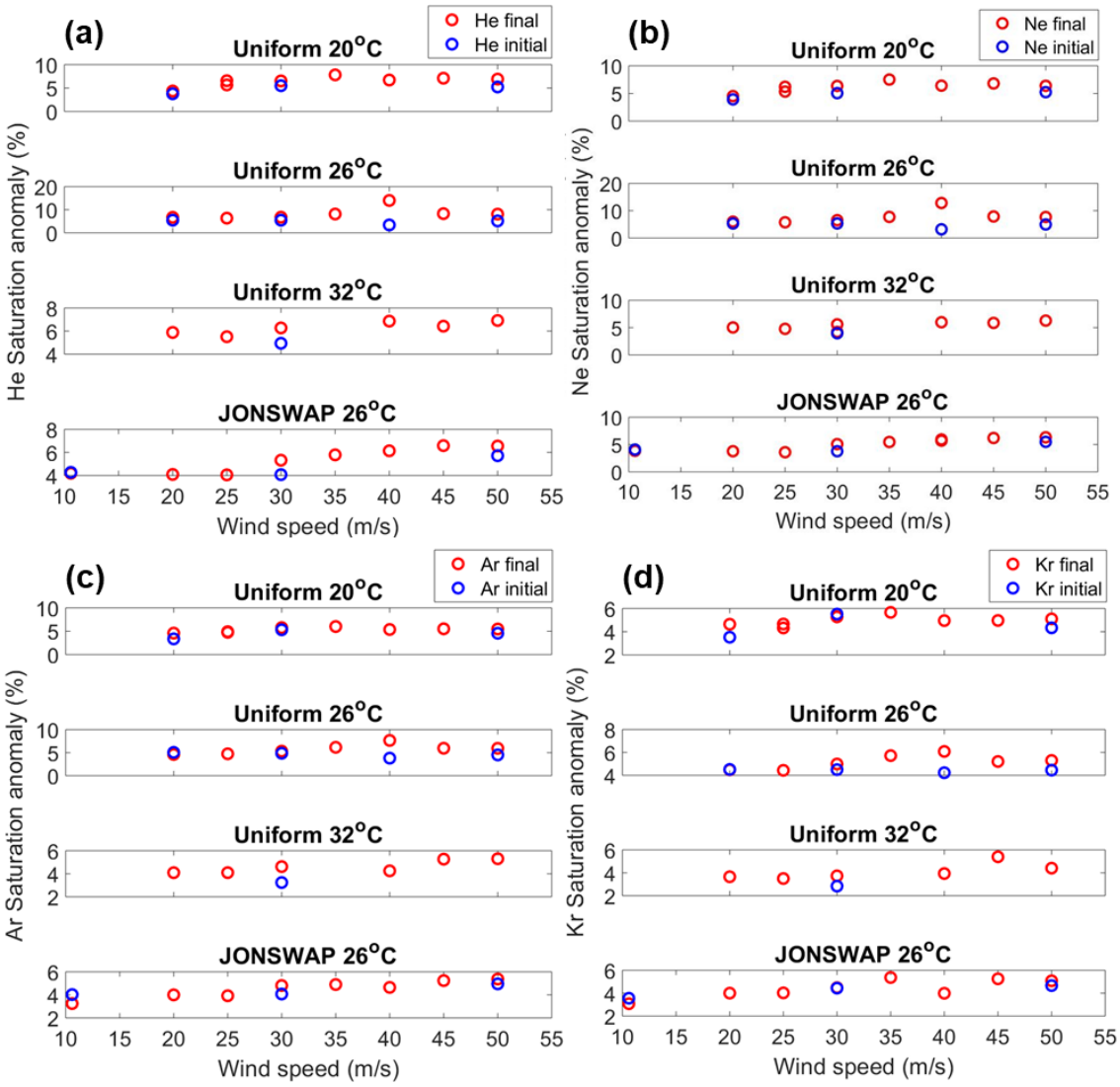

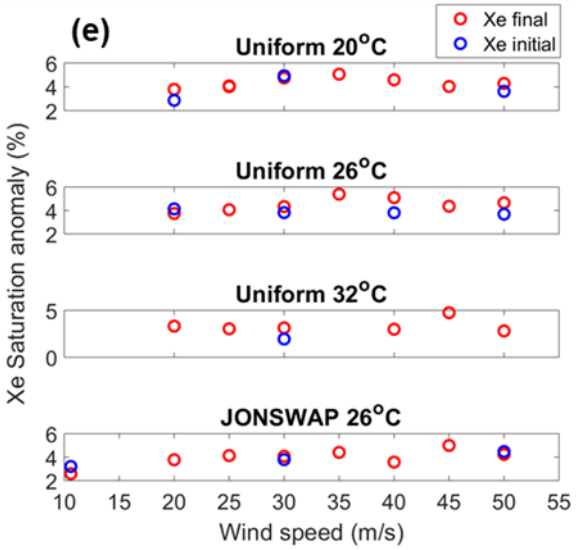

Figure 34. Saturation anomalies of (a) He, (b) Ne, (c) Ar, (d) Kr, and (e) Xe were calculated as a function of wind speed for all experiments not directly following after the tank water temperature change. Initial saturation anomalies are denoted in blue and the final in red.

4.3. Steady state discrete saturation anomaly result

The discrete noble gas saturation anomalies at steady state were plotted as a function of wind speed for the different wind, wave and temperature conditions (Figure 35). He and Ne, the two gases with the lowest solubilities and therefore most affected by bubble injection, are plotted with filled circles in blue and red, respectively. Overall, our data show that for the two highest saturation anomaly conditions—uniform waves at 26°C and 20°C—the steady state saturation anomalies of gases level off at higher wind speeds. The flattening of steady state saturation anomalies at high wind speeds was especially intriguing as it paralleled the behavior of momentum and heat flux transfer coefficients, which were shown to level off at high wind speeds (Haus et al., 2010). Since the steady state saturation anomaly does not necessarily correlate with gas flux, we must ultimately calculate the gas flux and to see whether it levels off at higher wind speed conditions. As a first step, the following sections explore the trend of discrete noble gases with temperature and bubbles as a function of wind speed to better understand the relationship between bubbles and gases at high wind speeds.

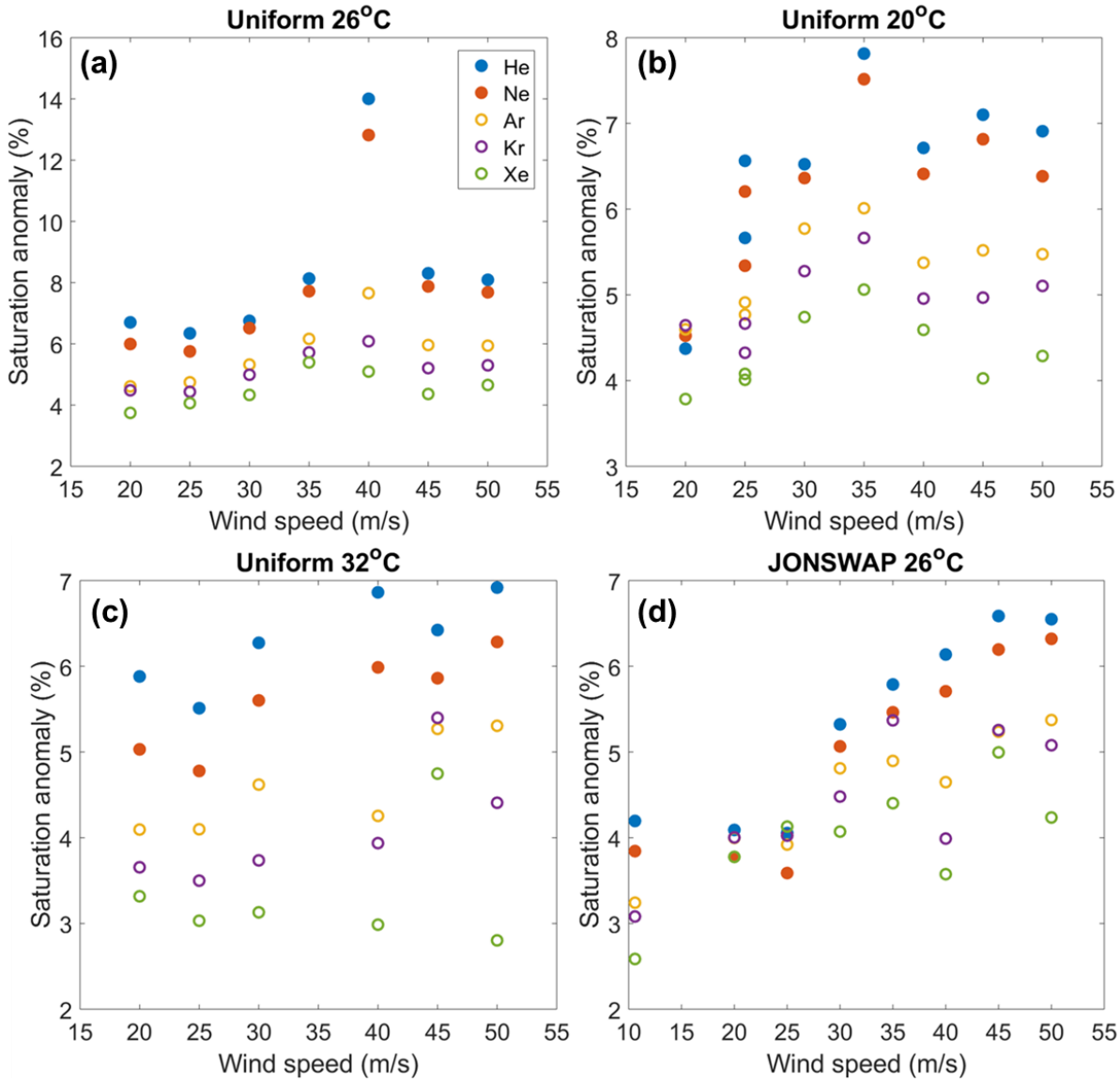

Figure 35. Saturation anomalies of five discrete noble gases (He, Ne, Ar, Kr, and Xe) from the end of each experiment are plotted as a function of wind speed for four different wave/temperature conditions: (a) uniform waves and water temperature of 26°C, (b) uniform waves and water temperature of 20°C, (c) uniform waves and average water temperature of 32°C, and (d) JONSWAP waves and average water temperature of 26°C.

4.3.1. Uniform waves

a. Trend with wind speed and temperature

For uniform wave conditions, saturation anomalies of noble gases were in the order

of He > Ne > Ar > Kr > Xe with very few exceptions (Figure 35). This result was not surprising, as we expected the least soluble gas to be most saturated due to bubble injection. Even the most soluble gas, Xe, was supersaturated which suggests to us that even Xe is affected by the bubble injection process at the wind speeds and wave conditions studied here. Across different temperatures, the general trend of supersaturation for He and Ne were in the order of 26°C > 20°C > 32°C for a given wind speed. For more soluble gases such as Ar, Kr, and Xe, at higher wind speeds, the same pattern of saturation anomaly and temperature trend (26°C > 20°C > 32°C) was observed. Interestingly, however, for Ar, Kr, and Xe at winds speeds 30 m s^{-1} and below, the saturation anomalies at a given wind speed was in the order of 20°C > 26°C > 32°C. This finding is really interesting because it points to the fact that bubble processes is related to temperature ordering. Below are figures of each noble gas plotted as a function of wind speed for the three different temperature conditions.

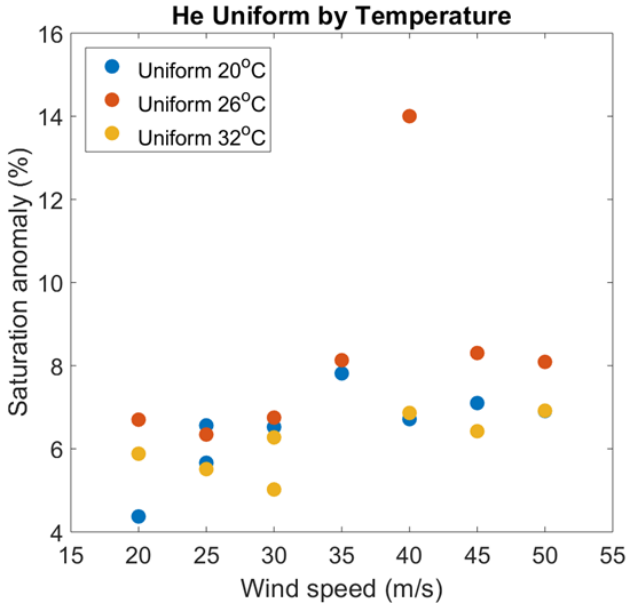

Figure 36. Saturation anomaly of discrete He at 26°C, 20°C, and 32°C as a function of wind speed. The saturation anomalies at a given wind speed were generally in the order of 26°C > 20°C > 32°C across different wind speeds. The datapoint for 50 m s^{-1} at 20°C is directly behind that at 32°C.

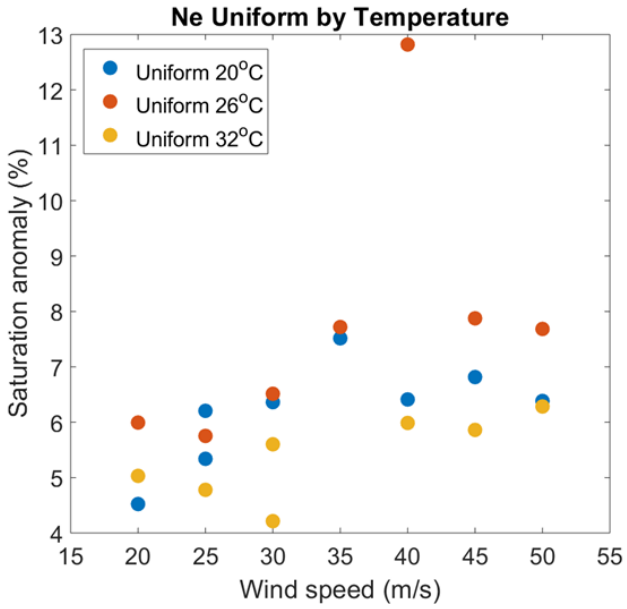

Figure 37. Saturation anomaly of Ne across water temperatures at 26°C, 20°C, and 32°C as a function of wind speed. The saturation anomalies at a given wind speed were generally in the order of 26°C > 20°C > 32°C, following a pattern seen for He.

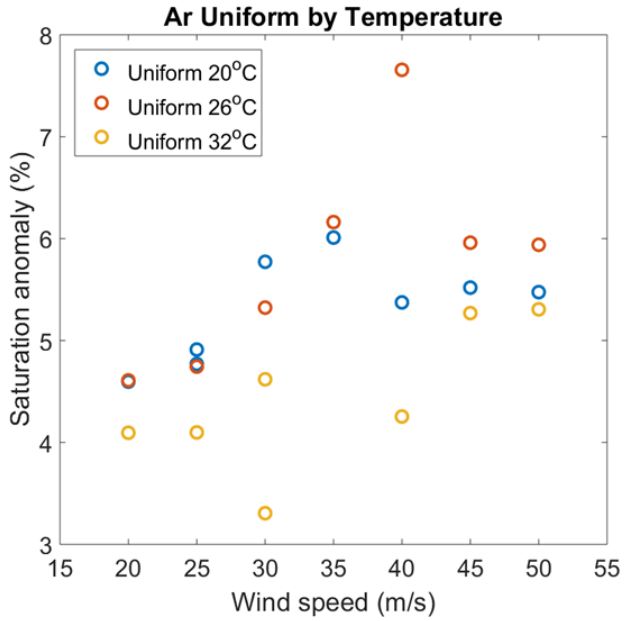

Figure 38. Saturation anomaly of Ar across water temperatures at 26°C, 20°C, and 32°C as a function of wind speed. The saturation anomalies at a given wind speed were in the order of 26°C > 20°C > 32°C for wind speeds over 40 m s^{-1}. At lower wind speeds, the 20°C condition had higher saturation anomaly than 26°C condition.

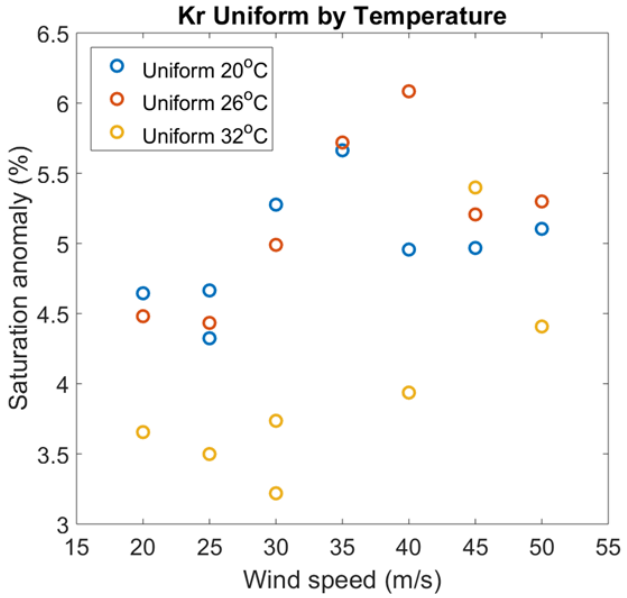

Figure 39. Saturation anomaly of Kr across water temperatures at 26°C, 20°C, and 32°C as a function of wind speed. The saturation anomalies at a given wind speed were in the order of 26°C > 20°C > 32°C for higher wind speeds 40 and 50 m s^{-1}. 20°C condition has higher saturation anomaly than 26°C condition for wind speeds at 30 m s^{-1} or lower.

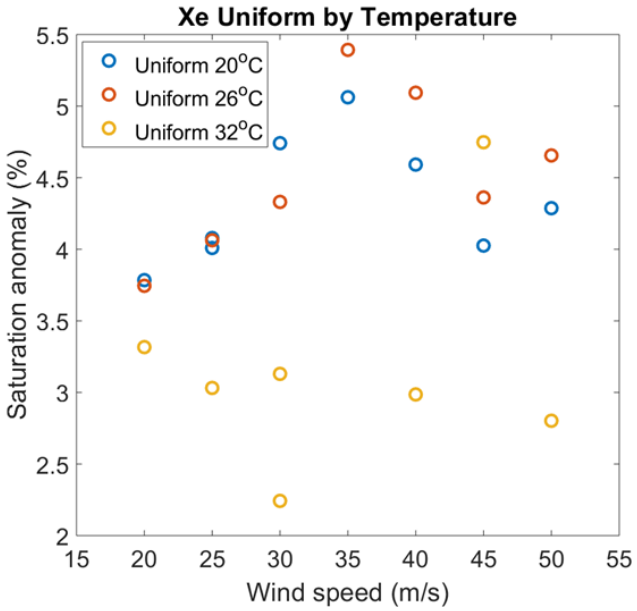

Figure 40. Saturation anomaly of Xe across water temperatures at 26°C, 20°C, and 32°C as a function of wind speed. The saturation anomalies at a given wind speed were in the order of 26°C > 20°C > 32°C for higher wind speeds 40 and 50 m s^{-1}. 20°C condition has higher saturation anomaly than 26°C condition for wind speeds at 30 m s^{-1} or lower.

Previous studies suggest that water temperature and steady state supersaturation due

to bubbles are inversely related (Liang et al., 2013). The chemical reasoning behind this relationship is that as water temperature increases, the molecular diffusivity of a gas increases while the viscosity of the water decreases. This results in the increase of total gas flux from diffusive gas exchange, which in turn, decreases the saturation anomaly as the outgoing gas flux tries to balance out the bubble-mediated supersaturation (which is less affected by molecular diffusivity changes because completely trapped bubbles inject all of their air, regardless of diffusivity). In our result, this relationship seems to hold true for relatively soluble gases at lower wind speeds, as the order for saturation anomalies was 20°C > 26°C > 32°C water temperature for wind speeds at or below 30 m s^{-1} for Ar, Kr, and Xe. Less soluble gases such as He and Ne, however, had saturation anomalies in the order of 26°C > 20°C > 32°C water temperature across all wind speeds. Similarly, even for more soluble gases such as Ar, Kr, and Xe the saturation anomaly at a given wind speed was largely in the order of 26°C > 20°C > 32°C water temperature at or above 35 m s^{-1}. Given that (1) less soluble gases such as He and Ne (i.e., gases that are most affected by bubble mediated gas exchange) had higher saturation anomaly at 26°C than at 20°C and that (2) relatively soluble gases also had unexpected water temperature and saturation anomaly relationship at higher wind speed, our result suggests that increased bubble flux may be playing an important role in altering the expected water temperature dependence of saturation anomaly.

As the water temperature increases, it is generally thought that the amount of gas flux from completely dissolving bubbles remains the same while the amount of gas flux from partially dissolving bubble and the gas flux from the interface increases (Liang et al., 2013). Thus, if there is a large contribution from partially dissolving bubbles, a higher temperature might result in a larger saturation anomaly due to this increased flux. One possible reason for our observation therefore is that there are two competing effects—one that would cause the bubble induced supersaturations to increase at warmer temperatures and one that would cause the bubble induced supersaturations to decrease at warmer temperatures. The results show an intermediate behavior with the middle temperature actually having the largest supersaturations. Once bubble size spectra have been processed for all the experiments, this hypothesis can be evaluated by examining the shift in sizes of bubbles at different

temperatures and wind speeds because larger bubbles are more affected by partial bubble trapping and smaller ones by complete dissolution.

Another possibility related to the above argument is that bubble entrainment and penetration may be temperature dependent, which is an assumption not considered in the proposed inverse relationship between water temperature and saturation anomaly (Liang et al., 2013). In fact, a study in the real ocean has shown that the turbulence dissipation rates were suppressed during periods of high downward heat flux into the ocean, which created large near-surface temperature gradients (Vagle et al., 2012). This suppression of turbulence dissipation led to decreased large bubbles with depth during the period of large heat flux.

b. Trend with wind speed and bubbles

Bubble data was analyzed in terms of surface area (Figure 41) and total volume (Figure 42) as a function of wind speed for uniform waves at 26°C water temperature. Additionally, the number of bubbles at a given radius was plotted for each of the experiments (Figure 43).

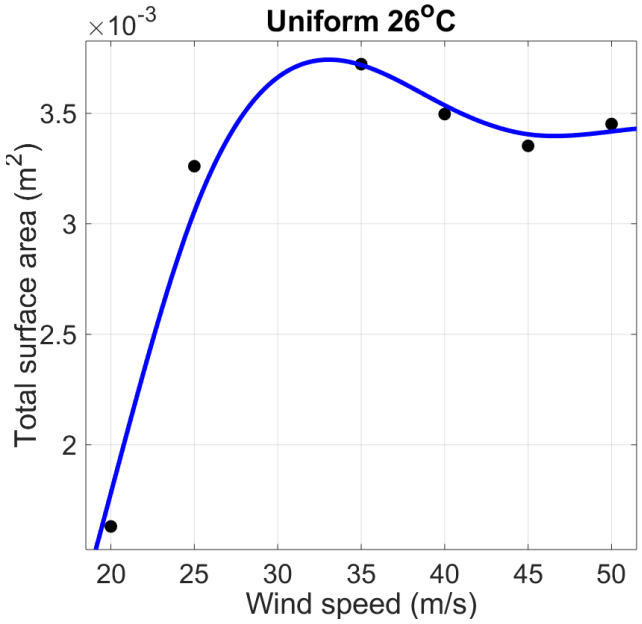

Figure 41. Total surface area of bubbles captured by the bubble imager as a function of wind speed for uniform waves at 26°C water temperature. Total surface area of the bubbles from 17 to 7 minutes before the end of each experiment was calculated. *Credit: Andrew Wyatt Smith, University of Miami SUSTAIN Laboratory, by personal communication.*

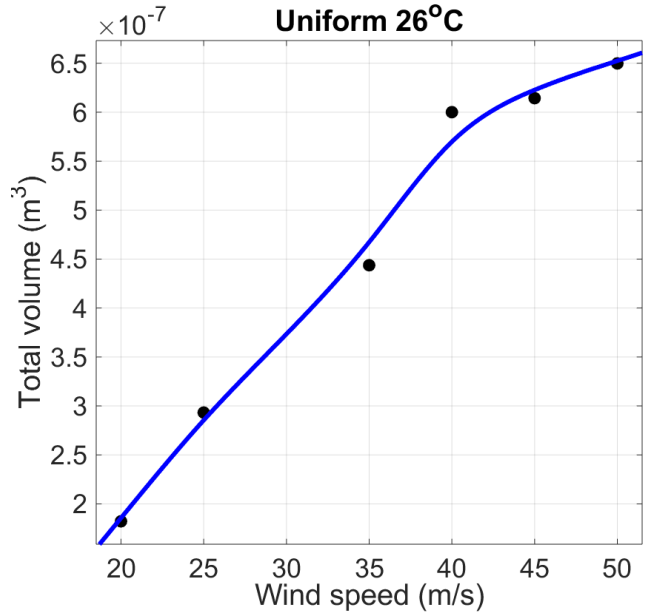

Figure 42. Total volume of bubbles captured by the bubble imager as a function of wind speed for uniform waves at 26°C water temperature. Total volume of the bubbles from 17 to 7 minutes before the end of each experiment was calculated. *Credit: Andrew Wyatt Smith, University of Miami SUSTAIN Laboratory, by personal communication.*

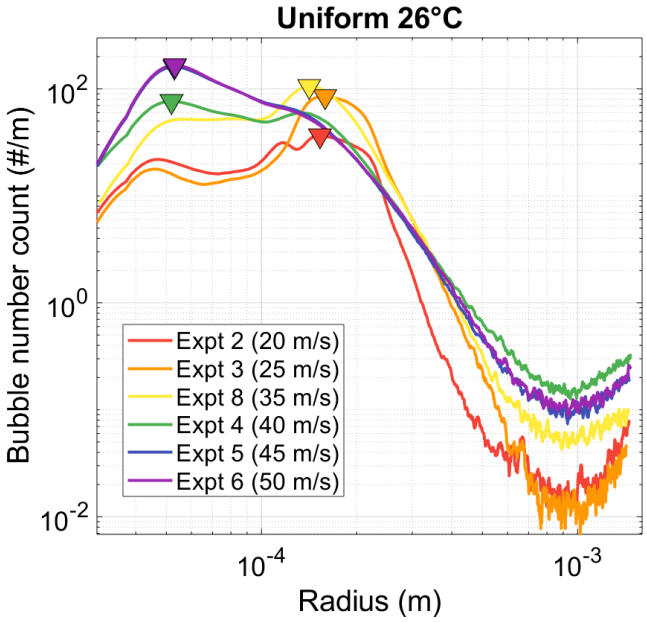

Figure 43. Average bubble number count as a function of bubble radius for experiments with uniform waves at 26°C water temperature. Lower wind speeds resulted in more intermediate sized bubbles and higher wind speeds resulted in more small and large bubbles. Both axes are on log scale. Downward triangles represent peak bubble number count for a given wind speed. *Credit: Andrew Wyatt Smith, University of Miami SUSTAIN Laboratory, by personal communication.*

The bubble volume incrementally increases as a function of wind speed (Figure 42) while the surface area peaks at 35 m s^{-1}, then decrease and flatten off at higher wind speeds (Figure 41). These results suggests that the peak of the discrete noble gas sample at 40 m s^{-1} (Figure 35 (a)) is likely due to the timing of sample collection and may not truly be reflecting a larger gas saturation anomaly—for uniform waves at 26°C water temperature condition, the discrete

noble gas sample at 40 m s^{-1} was taken right before the experiment ended, but for experiments at 45 and 50 m s^{-1} the samples were taken right after the experiment ended (see Table 1 and section 4.2.1.). The bubble data show that the slope of bubble volume increases as a function of wind speed at low and moderate wind speeds but then it remains steady or even decreases at higher wind speeds. For the discrete noble gases in uniform wave experiments at 20°C water temperature, the saturation anomalies leveled off similarly at the two highest wind speeds. Since the bubble data has not yet been processed for that series of experiments, it is not yet known whether the peak at 35 m s^{-1} is also related to increased bubble volume. For conditions with lower saturation anomalies, such as uniform waves at 32°C and JONSWAP waves, we see a more linear relationship between saturation anomaly and wind speed.

Given that saturation anomalies of gases at conditions that produce the highest saturation anomalies level off, it may be possible that at one point there is a limit on how much the water can be supersaturated by bubbles. However, the observed pattern may also be due to the shallowness of the tank, which could limit the extent of bubble dissolution. Since the water depth was at around 0.75 m, bubbles may not have had enough time to dissolve before they rose and reached the water surface. In fact, the similarity in the "leveling off" behavior between bubble surface area and noble gas saturation anomalies may be pointing to the importance of partially dissolving bubbles at high wind speeds. This is because partially dissolving bubbles are most sensitive to total surface area whereas completely trapped bubbles are most sensitive to bubble volume.

4.3.2. JONSWAP waves

The discrete steady states saturation anomalies of He and Ne slightly decreased while Kr and Xe increased between wind speeds 10.6 and 25 m s^{-1}. From wind speed 30 m s^{-1} up to 45 m s^{-1}, the saturation anomalies of He and Ne steadily increased; in between 45 m s^{-1} and 50 m s^{-1}, saturation anomaly of He dropped slightly while Ne slightly increased (Figure 35 (d)). The trends of other gases are more sporadic at wind speeds of 30 ms^{-1} and above. In general, the saturation anomaly of each gas is lower than the conditions with uniform waves. The results from Experiments 25 and 26 are excluded from the figure results

and discussion section because the wave settings were different from all the other experiments (all other JONSWAP experiments were at the setting 1 second peak period and 0.15 m wave amplitude). At higher wave amplitude settings, the gases resulted in higher saturation anomaly than the same wind speed experiment with lower wave amplitude settings. While this relationship is something that we have expected, it is a nice confirmation to see that wave energy is positively related to saturation states of the gases.

The figures showing total bubble surface area vs. wind speed (Figure 44), total bubble volume vs. wind speed (Figure 45), and bubble number count per radius vs. radius (Figure 46) for JONSWAP waves at 26°C water temperature are presented below.

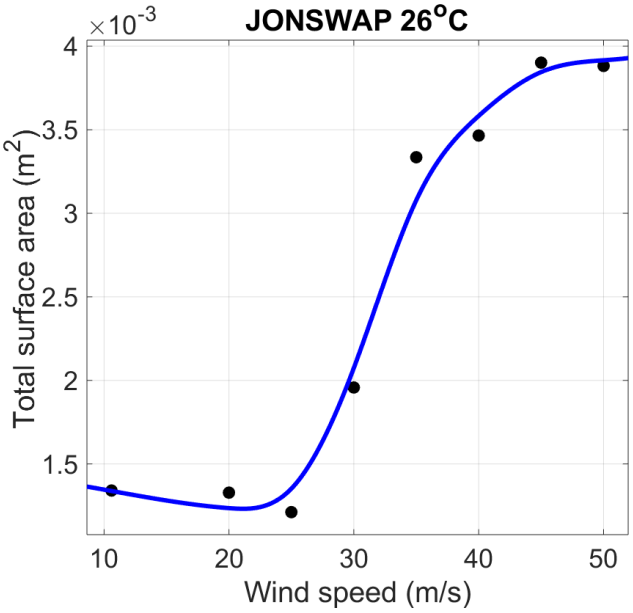

Figure 44. Total surface area of bubbles captured by the bubble imager as a function of wind speed for JONSWAP waves at 26°C water temperature. Total surface area of the bubbles from 17 to 7 minutes before the end of each experiment was calculated. *Credit: Andrew Wyatt Smith, University of Miami SUSTAIN Laboratory, by personal communication.*

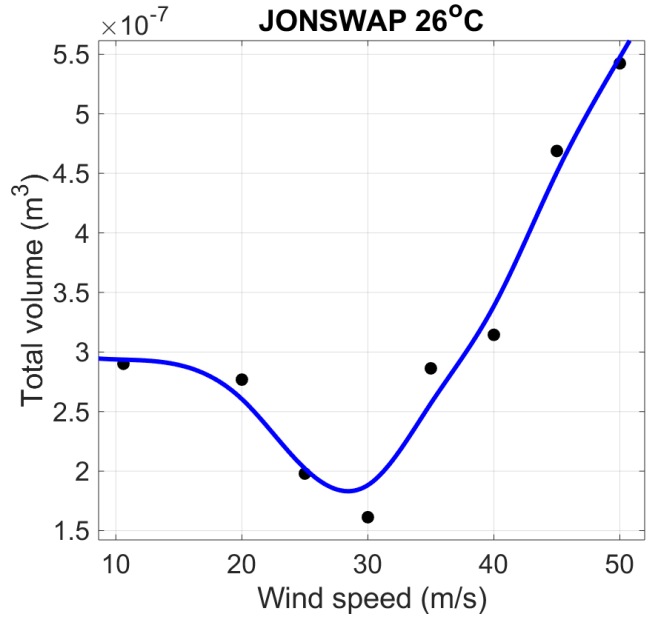

Figure 45. Total volume of bubbles captured by the bubble imager as a function of wind speed for JONSWAP waves at 26°C water temperature. Total volume of the bubbles from 17 to 7 minutes before the end of each experiment was calculated. *Credit: Andrew Wyatt Smith, University of Miami SUSTAIN Laboratory, by personal communication.*

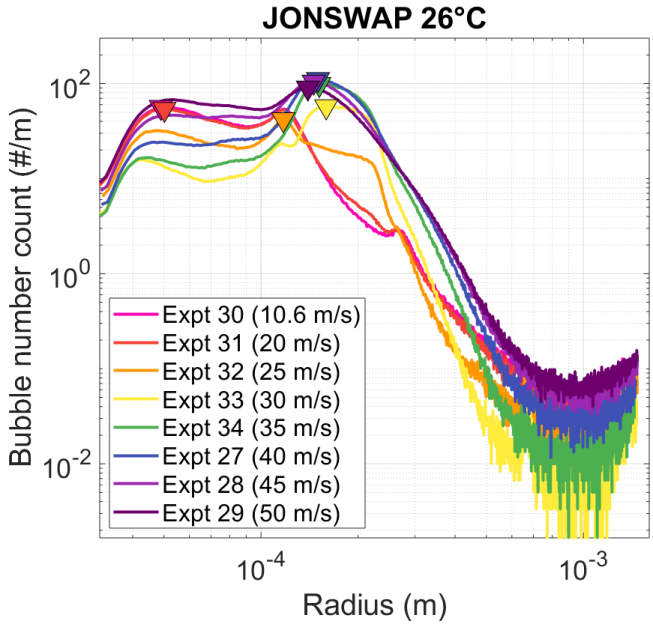

Figure 46. Bubble number count as a function of bubble radius for JONSWAP waves at 26°C water temperature. The most abundant bubble sizes are slightly larger at higher wind speeds than lower ones. Also, the largest bubbles occur more frequently at higher wind speeds. Both axes are on log scale. Downward triangles represent peak bubble number count for a given wind speed. *Credit: Andrew Wyatt Smith, University of Miami SUSTAIN Laboratory, by personal communication.*

Similar to what we observed for uniform waves at 26°C, the bubble surface area for JONSWAP waves at 26°C levels off at higher wind speed. However, the wind speed that the bubble surface area starts to level off at is higher in JONSWAP waves (40 vs. 45 m s^{-1}) than in the uniform case. Additionally, the pattern of bubble volume with respect to wind speed, especially above 30 m s^{-1}, is similar to the equilibrium saturation anomalies, just as was

observed for uniform waves. The fact that the saturation anomalies of He and Ne linearly increase with wind speed and do not flatten off completely (at least at the wind speed we observe) suggests that at higher wind speeds, there is a mixture of both partially and completely dissolving bubbles. The size distribution of uniform and JONSWAP spectrum at 26°C presents another interesting difference between the two wave types. Both uniform and JONSWAP waves have the two extreme ends of the bubble sizes—the large and the small—but JONSWAP waves also have more intermediate size bubbles and less of very small bubbles compared to uniform waves. It may be possible that more turbulent uniform waves produce larger bubbles that exceed the Hinze scale and therefore are fragmented into smaller bubbles (Deane and Stokes, 2002).

In conclusion, the unexpected saturation anomaly dependence on water temperature suggests the importance of flux contributions from partially dissolving bubbles. The noble gases also exhibited different saturation anomaly dependence on wind speeds between uniform and JONSWAP wave conditions. For uniform waves, the steady state saturation anomalies of gases leveled off at high wind speed. The “leveling off" behavior of saturation anomalies, however, was not observed for the JONSWAP waves, at least within the observed wind speed range. Finally, the similarity in the pattern between the bubble surface area data and the steady state saturation anomalies at high wind speeds suggests the importance of partially dissolving bubbles, especially in the case of uniform waves.

Chapter 5. Conclusion

The good agreement between the continuous Ne/Xe saturation anomaly record and the bubble volume data shows that GEMS is a highly reliable method to quantify bubble-mediated gas exchange in real time. Additionally, GEMS and discrete noble gas results involving prior warming/cooling of the tank water suggest that steady state saturation anomalies are most likely independent of the initial conditions. Analysis of discrete noble gas results for different wave conditions at 26°C water temperature shows that the saturation anomalies for uniform waves level off at higher wind speeds. A similar pattern, however, was not observed for JONSWAP waves, at least for the range of wind speeds used in our

experiments.

In addition, two aspects of our result highlight the importance of flux contribution from partially dissolving bubbles especially for uniform waves. First, our result presented an unexpected temperature dependence of steady state saturation anomalies. For a given wind speed, the condition with intermediate water temperature resulted in the highest saturation anomaly for He and Ne (this was also true for other gases at higher wind speeds)—contrary to the expected inverse relationship between temperature and saturation anomaly. We hypothesize that this may be due to the flux contribution from partially dissolving bubbles, which increases with temperature. Second, the total bubble surface area data and the steady state gas saturation anomalies both leveled off at high wind speeds for uniform waves at 26°C water temperature. Since flux contribution from partially dissolving bubbles can be best tracked by the bubble surface area, this may be another piece of evidence supporting the importance of partially dissolving bubbles at high wind speeds. The shallowness of the tank, however, could be contributing to this result as bubbles may not have had enough time to dissolve before they reached the water surface.

As the next step, we will construct a box model to calculate the gas flux and steady state saturation anomaly with small time steps. By doing so, we will be able to quantitatively explore the relationship between gas flux and wind speed—on one hand, a few studies conducted at high wind speeds showed that gas flux increased dramatically as wind speed increased (Iwano et al., 2013; McNeil and D'Asaro, 2007; Mesarchaki et al., 2015). On the other hand, momentum and heat flux transfer coefficients were shown to level off at around 30 m s^{-1} (Haus et al., 2010) and so it will be very interesting to see whether gas fluxes level off in our experiments. In order to calculate the flux, we will need to calculate how the concentration of the noble gases change with time by combining the mole ratios from the GEMS with the oxygen concentration data obtained from an optode and the O_2/Ar ratios obtained from the Equilibration Inlet Mass Spectrometer (EIMS).

We also hope to examine parameters influencing bubble mediated gas exchange, such as the difference in flux contribution from completely vs. partially dissolving bubbles. Additionally, we would like to see how other physical measurements such as wave height,

wave spectral slope, turbulent kinetic energy, etc. affect both diffusive gas exchange and bubble-mediated gas exchange. Finally, if we were to conduct another set of experiments at a wind-wave tank, it would be interesting to look at the steady state saturation anomalies of JONSWAP waves at wind speeds higher than 50 m s^{-1} to see whether those eventually level off as was the case for uniform waves.

References

Alfred C. Glassell Jr. SUSTAIN Laboratory, 2015. Facility.

Asher, W., Karle, L., Higgins, B., Farley, P., Monahan, E., Leifer, I., 1996. The influence of bubble plumes on air-seawater gas transfer velocities. J. Geophys. Res. 101, 12027-12041.

Carpenter, L.J., Archer, S.D., Beale, R., 2012. Ocean-atmosphere trace gas exchange. Chem. Soc. Rev. 41, 6473-6506.

Cassar, N., Barnett, B.A., Bender, M.L., Kaiser, J., Hamme, R.C., Tilbrook, B., 2009. Continuous high-frequency dissolved O_2/Ar measurements by equilibrator inlet mass spectrometry. Anal. Chem. 81, 1855-1864.

Craig, H., Hayward, T., 1987. Oxygen Supersaturation in the Ocean: Biological Versus Physical Contributions. Science 235, 199-202.

Deane, G.B., Stokes, M.D., 2002. Scale dependence of bubble creation mechanisms in breaking waves. Nature 418, 839-844.

Goddijn-Murphy, L., Woolf, D.K., Callaghan, A.H., Nightingale, P.D., Shutler, J.D., 2016. A reconciliation of empirical and mechanistic models of the air-sea gas transfer velocity. J. Geophys. Res. 121, 818-835.

Hamme, R.C., Cassar, N., Lance, V.P., Vaillancourt, R.D., Bender, M.L., Strutton, P.G., Moore, T.S., DeGrandpre, M.D., Sabine, C.L., Ho, D.T., 2012. Dissolved O_2/Ar and other methods reveal rapid changes in productivity during a Lagrangian experiment in the Southern Ocean. J. Geophys. Res. 117.

Hamme, R.C., Emerson, S.R., 2006. Constraining bubble dynamics and mixing with dissolved gases: Implications for productivity measurements by oxygen mass balance. J. Mar. Res. 64, 73-95.

Hamme, R.C., Severinghaus, J.P., 2007. Trace gas disequilibria during deep-water formation. Deep Sea Res., Part I. 54, 939-950.

Haus, B.K., Jeong, D., Donelan, M.A., Zhang, J.A., Savelyev, I., 2010. Relative rates of sea-air heat transfer and frictional drag in very high winds. Geophys. Res. Lett. 37.

Ho, D.T., Law, C.S., Smith, M.J., Schlosser, P., Harvey, M., Hill, P., 2006. Measurements of air-sea gas exchange at high wind speeds in the Southern Ocean: Implications for global parameterizations. Geophys. Res. Lett. 33.

Iwano, K., Takagaki, N., Kurose, R., Komori, S., 2013. Mass transfer velocity across the breaking air–water interface at extremely high wind speeds. Tellus B: Chem. Phys. Meteorol. 65, 21341.

Jenkins, W., 1988. The use of anthropogenic tritium and helium-3 to study subtropical gyre ventilation and circulation. Philos. Trans. R. Soc. Lond. Ser. A-Math. Phys. Eng. Sci. 325, 43-61.

Johnson, M.T., 2010. A numerical scheme to calculate temperature and salinity dependent air-water transfer velocities for any gas. Ocean Sci. 6, 913-932.

Keeling, C.D., Piper, S.C., Bacastow, R.B., Wahlen, M., Whorf, T.P., Heimann, M., Meijer, H.A., 2019. Scripps CO_2 measurements. Scripps Institution of Oceanography.

Krall, K., Jähne, B., 2014. First laboratory study of air–sea gas exchange at hurricane wind speeds. Ocean Sci. 10, 257-265.

Krevanko, C., 2018. Improving Models for Air-Sea Gas Exchange using measurements of Noble Gas ratios in a Wind-Wave Tank.

Leifer, I., Patro, R.K., 2002. The bubble mechanism for methane transport from the shallow sea bed to the surface: A review and sensitivity study. Cont. Shelf Res. 22, 2409-2428.

Liang, J.H., Deutsch, C., McWilliams, J.C., Baschek, B., Sullivan, P.P., Chiba, D., 2013. Parameterizing bubble-mediated air-sea gas exchange and its effect on ocean ventilation. Global Biogeochem. Cyc. 27, 894-905.

Liss, P.S., Merlivat, L., 1986. Air-sea gas exchange rates: Introduction and synthesis, in: Buat-Ménard, P. (Ed.), The role of air-sea exchange in geochemical cycling. Springer, pp. 113-127.

Manning, C.C., Stanley, R.H., Lott III, D.E., 2016. Continuous measurements of dissolved Ne, Ar, Kr, and Xe ratios with a field-deployable gas equilibration mass spectrometer. Anal. Chem. 88, 3040-3048.

McGillis, W.R., Edson, J., Hare, J., Fairall, C., 2001. Direct covariance air-sea CO_2 fluxes.

J. Geophys. Res. 106, 16729-16745.

McNeil, C., D'Asaro, E., 2007. Parameterization of air–sea gas fluxes at extreme wind speeds. J. Mar. Syst. 66, 110-121.

Mesarchaki, E., Kräuter, C., Krall, K., Bopp, M., Helleis, F., Williams, J., Jähne, B., 2015. Measuring air–sea gas-exchange velocities in a large-scale annular wind–wave tank. Ocean Sci. 11, 121-138.

Nightingale, P.D., Malin, G., Law, C.S., Watson, A.J., Liss, P.S., Liddicoat, M.I., Boutin, J., Upstill-Goddard, R.C., 2000. In situ evaluation of air-sea gas exchange parameterizations using novel conservative and volatile tracers. Global Biogeochem. Cyc. 14, 373-387.

Petit, J.-R., Jouzel, J., Raynaud, D., Barkov, N.I., Barnola, J.-M., Basile, I., Bender, M., Chappellaz, J., Davis, M., Delaygue, G., 1999. Climate and atmospheric history of the past 420,000 years from the Vostok ice core, Antarctica. Nature 399, 429.

Pozzer, A., Jöckel, P., Sander, R., Williams, J., Ganzeveld, L., Lelieveld, J., 2006. Technical Note: The MESSy-submodel AIRSEA calculating the air-sea exchange of chemical species. Atmos. Chem. Phys. 6, 5435-5444.

Sabine, C.L., Feely, R.A., Gruber, N., Key, R.M., Lee, K., Bullister, J.L., Wanninkhof, R., Wong, C., Wallace, D.W., Tilbrook, B., 2004. The oceanic sink for anthropogenic CO_2. Science 305, 367-371.

Spitzer, W.S., Jenkins, W.J., 1989. Rates of vertical mixing, gas exchange and new production: Estimates from seasonal gas cycles in the upper ocean near Bermuda. J. Mar. Res. 47, 169-196.

Stanley, R.H., Jenkins, W.J., 2013. Noble gases in seawater as tracers for physical and biogeochemical ocean processes, The Noble Gases as Geochemical Tracers. Springer, pp. 55-79.

Stanley, R.H., Kirkpatrick, J.B., Cassar, N., Barnett, B.A., Bender, M.L., 2010. Net community production and gross primary production rates in the western equatorial Pacific. Global Biogeochem. Cyc. 24.

Stanley, R.H.R., Baschek, B., Lott, D.E., Jenkins, W.J., 2009a. A new automated method for measuring noble gases and their isotopic ratios in water samples. Geochemistry Geophysics Geosystems 10, 18.

Stanley, R.H.R., Jenkins, W.J., Lott, D.E., Doney, S.C., 2009b. Noble gas constraints on air-sea gas exchange and bubble fluxes. Journal of Geophysical Research-

Oceans 114, 14.

Vagle, S., Gemmrich, J., Czerski, H., 2012. Reduced upper ocean turbulence and changes to bubble size distributions during large downward heat flux events. J. Geophys. Res. 117.

Vagle, S., McNeil, C., Steiner, N., 2010. Upper ocean bubble measurements from the NE Pacific and estimates of their role in air-sea gas transfer of the weakly soluble gases nitrogen and oxygen. J. Geophys. Res. 115.

Wanninkhof, R., 1992. Relationship between wind speed and gas exchange over the ocean. J. Geophys. Res. 97, 7373-7382.

Wanninkhof, R., Asher, W.E., Ho, D.T., Sweeney, C., McGillis, W.R., 2009. Advances in quantifying air-sea gas exchange and environmental forcing.

Wanninkhof, R., McGillis, W.R., 1999. A cubic relationship between air-sea CO_2 exchange and wind speed. Geophys. Res. Lett. 26, 1889-1892.

Weiss, R., 1968. Piggyback sampler for dissolved gas studies on sealed water samples, Deep Sea Res. Oceanogr. Abstr. Elsevier, pp. 695-699.

Woolf, D., Leifer, I., Nightingale, P., Rhee, T., Bowyer, P., Caulliez, G., De Leeuw, G., Larsen, S.E., Liddicoat, M., Baker, J., 2007. Modelling of bubble-mediated gas transfer: Fundamental principles and a laboratory test. J. Mar. Syst. 66, 71-91.